9-25-2019

Polar Alignment of a Protoplanetary Disc Around an Eccentric Binary – III. Effect of Disc Mass

Rebecca G. Martin
University of Nevada, Las Vegas, rebecca.martin@unlv.edu

Stephen H. Lubow
Space Telescope Science Institute

Monthly Notices
of the
ROYAL ASTRONOMICAL SOCIETY

MNRAS **490,** 1332–1349 (2019)
Advance Access publication 2019 September 25

doi:10.1093/mnras/stz2670

Polar alignment of a protoplanetary disc around an eccentric binary – III. Effect of disc mass

Rebecca G. Martin [1]★ and Stephen H. Lubow [2]

[1] *Department of Physics and Astronomy, University of Nevada, Las Vegas, 4505 South Maryland Parkway, Las Vegas, NV 89154, USA*
[2] *Space Telescope Science Institute, 3700 San Martin Drive, Baltimore, MD 21218, USA*

Accepted 2019 September 17. Received 2019 August 22; in original form 2019 April 25

ABSTRACT

An initially sufficiently misaligned low-mass protoplanetary disc around an eccentric binary undergoes damped nodal oscillations of tilt angle and longitude of ascending node. Dissipation causes evolution towards a stationary state of polar alignment in which the disc lies perpendicular to the binary orbital plane with angular momentum aligned to the eccentricity vector of the binary. We use hydrodynamic simulations and analytical methods to investigate how the mass of the disc affects this process. The simulations suggest that a disc with non-zero mass settles into a stationary state in the frame of the binary, the generalized polar state, at somewhat lower levels of misalignment with respect to the binary orbital plane, in agreement with the analytical model. Provided that discs settle into this generalized polar state, the observational determination of the misalignment angle and binary properties can be used to determine the mass of a circumbinary disc. We apply this constraint to the circumbinary disc in HD 98800. We obtain analytical criteria for polar alignment of a circumbinary ring with mass that approximately agree with the simulation results. Very broad misaligned discs undergo breaking, but the inner regions at least may still evolve to a polar state. The long-term evolution of the disc depends on the evolution of the binary eccentricity that we find tends to decrease. Although the range of parameters required for polar alignment decreases somewhat with increasing disc mass, such alignment appears possible for a broad set of initial conditions expected in protostellar circumbinary discs.

Key words: accretion, accretion discs – hydrodynamics – planets and satellites: formation – binaries: general.

1 INTRODUCTION

During the star formation process, misaligned discs around binary stars may be formed through chaotic accretion (e.g. Bate, Bonnell & Bromm 2003; McKee & Ostriker 2007; Monin et al. 2007; Bate, Lodato & Pringle 2010; Bate 2018) or stellar flybys (Clarke & Pringle 1993; Xiang-Gruess 2016; Cuello et al. 2019). Observations of circumbinary discs suggest misalignments may be common (e.g. Chiang & Murray-Clay 2004; Winn et al. 2004; Capelo et al. 2012; Kennedy et al. 2012; Brinch et al. 2016; Aly, Lodato & Cazzoletti 2018; Aronow et al. 2018; Czekala et al. 2019). The planet formation process in these discs will be altered by the torque from the binary that is not present in the single star case (e.g. Nelson 2000; Mayer et al. 2005; Boss 2006; Martin et al. 2014; Fu, Lubow & Martin 2015a,b, 2017; Franchini, Martin & Lubow 2019a). Furthermore, giant planets that form in a misaligned disc may no longer remain coplanar to the disc (Picogna & Marzari 2015; Lubow & Martin 2016; Martin et al. 2016). In order to understand the observed properties of exoplanets, we first need to explain the disc evolution in misaligned systems.

A misaligned circumbinary disc around a *circular* orbit binary undergoes uniform nodal precession with constant tilt. The angular momentum vector of the disc precesses about the binary angular momentum vector. For a sufficiently warm and compact disc, the disc precesses as a solid body (e.g. Larwood & Papaloizou 1997). Dissipation within the disc leads to alignment with the binary orbital plane (Papaloizou & Terquem 1995; Lubow & Ogilvie 2000; Nixon, King & Pringle 2011; Nixon 2012; Facchini, Lodato & Price 2013; Lodato & Facchini 2013; Foucart & Lai 2013, 2014).

Massless (test) particles that orbit around an eccentric orbit binary can undergo nodal libration oscillations of the tilt angle and the longitude of the ascending node, if the particle's orbital plane is sufficiently misaligned with the binary's orbital plane (e.g. Verrier & Evans 2009; Farago & Laskar 2010; Doolin & Blundell 2011). Rather than precessing about the angular momentum vector of the

★ E-mail: rebecca.martin@unlv.edu

binary, such particles instead precess about the eccentricity vector of the binary.

Recently, we found that a low-mass warm protostellar circumbinary disc around an eccentric orbit binary can evolve towards polar (perpendicular) alignment with respect to the binary orbital plane for sufficiently high initial inclination (Martin & Lubow 2017). The tilt evolution occurs due to damping of the libration oscillations by dissipation in the disc and the disc angular momentum aligns to the eccentricity vector of the binary. Aly et al. (2015) found that cool discs that orbit binary black hole systems can also undergo such oscillations and polar alignment. This mechanism operates for sufficiently large misalignment angle (Aly et al. 2015; Lubow & Martin 2018; Zanazzi & Lai 2018).

In Lubow & Martin (2018) and Martin & Lubow (2018), with analytical and numerical models, we extended the parameter space studied to include different disc properties such as viscosity, temperature, size, and inclination, and binary properties such as eccentricity and binary mass ratio. For low initial inclination, a disc around an *eccentric* orbit binary undergoes tilt oscillations and non-uniform precession as it evolves towards alignment with the binary angular momentum vector (Smallwood et al. 2019).

For an orbiting particle with significant mass, the mass of this body has an important effect on the evolution of the system because it can affect the binary orbit, unlike in the low-mass or test particle case. This regime has previously been explored analytically (Lidov & Ziglin 1976; Ferrer & Osacar 1994; Farago & Laskar 2010; Zanazzi & Lai 2018). They found that the stationary misalignment alignment angle (fixed point) between the binary and particle orbital planes is reduced below 90° and depends on the binary eccentricity and the particle angular momentum. Although mass of a protostellar disc is much less than the mass of the binary, a circumbinary disc can extend to an outer radius that is much greater than the binary separation. Consequently, the angular momentum of a circumbinary disc can sometimes be significant compared to the binary angular momentum.

In this work, we explore for the first time the polar evolution of a circumbinary disc with significant mass around an eccentric binary by means of hydrodynamic simulations. We compare those results to the results for circumbinary particles with mass that effectively represent a ring with mass. The behaviour of a circumbinary particle or ring with mass provides some insight into the behaviour of discs. However, the disc is an extended object that experiences larger torques at smaller radii, while its angular momentum is typically dominated by material at larger radii. In addition, for the case of a disc with significant mass, the binary orbital properties, such as its eccentricity and semimajor axis, evolve due to two effects: first, the tidal interaction with the disc, and second, the accretion of circumbinary disc material.

In Section 2, we explore the evolution of a misaligned circumbinary disc with significant disc mass by means of hydrodynamic simulations. In Section 3, we consider a model of a ring with mass and obtain analytical expressions for the (generalized) polar inclination and the requirements for evolution to the polar state. We discuss the applications of our results in Section 4 and we draw conclusions in Section 5.

2 CIRCUMBINARY DISC SIMULATIONS

In this section, we explore the evolution misaligned circumbinary disc with significant mass around a binary star system. We apply the smoothed particle hydrodynamics (SPH; e.g. Price 2012, 2007) code PHANTOM (Lodato & Price 2010; Price & Federrath 2010; Price et al. 2018) that has been used extensively for simulations of misaligned accretion discs (e.g. Nixon 2012; Nixon, King & Price 2013; Martin et al. 2014; Fu et al. 2015a).

2.1 Simulation set-up

Table 1 summarizes the parameters and some results for all of the simulations that we describe in this section. The binary has components with masses $M_1 = M_2 = 0.5\,M$, where the total mass is $M = M_1 + M_2$. The binary orbits with semimajor axis $a_{\rm b}$ and eccentricity vector $\boldsymbol{e_{\rm b}} = (e_{x{\rm b}}, e_{y{\rm b}}, e_{z{\rm b}})$. The binary orbit is initially in the $x-y$ plane with eccentricity vector $\boldsymbol{e_{\rm b}} = (1, 0, 0)$. This $x-y$ plane serves as a reference plane for the orbital elements described below. The binary begins at apastron separation.

Initially the circumbinary disc is misaligned to the binary orbital plane by inclination angle i. The surface density is initially distributed by a power law $\Sigma \propto R^{-3/2}$ between the initial inner radius $R_{\rm in} = 2\,a_{\rm b}$ up to the initial outer radius $R_{\rm out}$. Typically we take $R_{\rm out} = 5\,a_{\rm b}$, but we do consider some larger values also. The initial inner disc truncation radius is chosen to be that of a tidally truncated coplanar disc (Artymowicz & Lubow 1994). However, the disc spreads both inwards and outwards during the simulation. As described in Lubow & Martin (2018), the inner edge of the disc extends closer to the binary because the usual gap-opening Lindblad resonances are much weaker on a polar disc around an eccentric binary than in a coplanar disc around a circular or eccentric orbit binary (see also Lubow, Martin & Nixon 2015; Miranda & Lai 2015; Nixon & Lubow 2015). We take the Shakura & Sunyaev (1973) α parameter to be 0.01 in our simulations. The disc viscosity is implemented in the usual manner by adapting the SPH artificial viscosity according to Lodato & Price (2010). The disc is locally isothermal with sound speed $c_{\rm s} \propto R^{-3/4}$ and the disc aspect ratio varies with radius as $H/R \propto R^{-1/4}$. Hence, α and the smoothing length $\langle h \rangle / H$ are constant over the radial extent of the disc (Lodato & Pringle 2007). We take $H/R = 0.1$ at $R_{\rm in} = 2\,a_{\rm b}$. We examined the effects of these two parameters in Lubow & Martin (2018). Particles in the simulation are removed if they pass inside the accretion radius for each component of the binary at $0.25\,a_{\rm b}$.

We ignore the effects of self-gravity in our calculations. Self-gravity can play an important role in cases where apsidal precession plays an important role in eccentric discs, as occurs for Kozai–Lidov discs (Batygin, Morbidelli & Tsiganis 2011; Fu et al. 2017). However, for an initially circular disc, as we assume, we find that the discs remain quite circular, as is expected since eccentricity is a constant of motion for ballistic circumbinary particles (in the quadrupole approximation) (Farago & Laskar 2010). Instead, nodal precession plays the key role in the dynamics of circumbinary discs. But self-gravity has no effect on the nodal precession rate of a flat disc. Provided that the disc is flat, the stationary tilt condition that we describe in Section 3.2 should be independent of self-gravity.

Self-gravity could have some influence on the level of warping and that in turn could affect the tilt evolution time. Narrow discs are more likely to be affected by self-gravity for a fixed disc mass, since the surface density is higher. However, the initial Toomre parameter is $Q > 2.3$ over the radial extent of the disc for the narrowest ($R_{\rm out} = 5\,a_{\rm b}$), highest disc mass ($M_{\rm d} = 0.05\,M$) that we consider. The value of Q increases over time in our simulations. Discs of larger radial extent that warp or break may be affected by self-gravity. However, the wider discs we consider have larger initial Toomre parameter $Q > 3.1$ for initial disc outer radius of $20\,a_{\rm b}$, and in the regions that warping or breaking

Table 1. Parameters of the initial circumbinary disc set up for binary with total mass M and separation a. The disc may be in a circulating (C) or librating (L) state.

Name	Figure	M_d/M	i (°)	e_b	R_{out}/a_b	C/L	Number of particles	Broken
run1	2	0.001	60	0.5	5	L	300 000	No
run2	2	0.01	60	0.5	5	L	300 000	No
run3	2	0.02	60	0.5	5	L	300 000	No
run4	2	0.05	60	0.5	5	L	300 000	No
run5	6	0.05	0	0.5	5	–	300 000	No
run6	6	0.01	0	0.5	5	–	300 000	No
run7	6	0.001	0	0.5	5	–	300 000	No
run8	7	0.05	20	0.5	5	C	300 000	No
run9	7	0.05	40	0.5	5	C	300 000	No
run10	7	0.05	50	0.5	5	C	300 000	No
run11	7	0.05	80	0.5	5	L	300 000	No
run12	8	0.05	20	0.8	5	C	300 000	No
run13		0.05	30	0.8	5	C	300 000	No
run14	8	0.05	40	0.8	5	L	300 000	No
run15	8	0.05	60	0.8	5	L	300 000	No
run16	8	0.05	80	0.8	5	L	300 000	No
run17	9	0.001	60	0.5	10	L	600 000	No
run18	9	0.01	60	0.5	10	L	600 000	No
run19	9	0.02	60	0.5	10	L	600 000	No
run20	9	0.05	60	0.5	10	L	600 000	No
run21	10	0.05	60	0.5	20	L	600 000	Yes

takes place, $Q \gtrsim 10$. Thus, self-gravity is not important in our calculations.

In order to present a large number of simulations in this work, we choose to use 3×10^5 particles in most of our following simulations. We found this number to provide sufficient resolution in fig. 1 in Martin & Lubow (2018) for a time of about 1000 P_{orb}, where P_{orb} is the orbital period of the binary. Fig. 1 shows the results of a similar resolution study, but for a disc with more mass. In the previous work, the convergence test started with a disc mass of $0.001\,M$, while in this study we use run4 of Table 1 in which the initial disc mass is $0.05\,M$. We find that the properties based on the first two oscillations are fairly well converged, based on the simulations with 3×10^5 and 1×10^6 particles. Lower resolution at late times leads to increased viscosity and more damping in the oscillations. But the behaviour in the two cases is quite similar in that the oscillations are centred about a binary-disc inclination $i_{bd} \sim 65°$, rather than almost 90° found for the lower mass disc in the earlier paper.

In order to provide adequate vertical resolution for a disc, we generally require that the smoothing length h be less than the disc scale height H (e.g. Armitage & Livio 1996). The disc is resolved with initial shell-averaged smoothing length per scale height $\langle h \rangle / H \approx 0.25$ for $R_{out} = 5\,a_b$. For simulations with larger initial disc outer radii $R_{out} = 10\,a_b$ and $R_{out} = 20\,a_b$, we use 6×10^5 particles initially and the disc is initially resolved with $\langle h \rangle / H \approx 0.26$ and $\langle h \rangle / H \approx 0.31$, respectively. The value of $\langle h \rangle / H$ does not change significantly over the disc over the times we simulate, as we show later.

A limitation of our simulations is that the flow in the central gap region is not well resolved by the SPH code in these intrinsically 3D flows. The flow in that region takes the form of rapid low-density gas streams (e.g. Artymowicz & Lubow 1996; Muñoz, Miranda & Lai 2019; Mösta, Taam & Duffell 2019). This limitation introduces some uncertainty in the binary evolution.

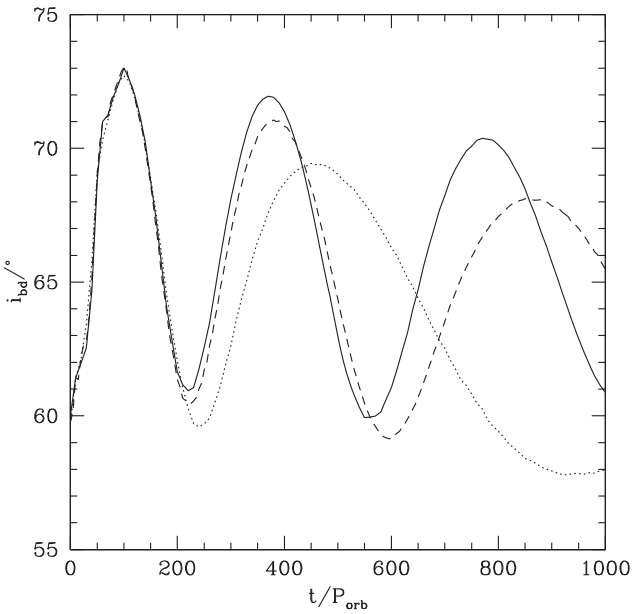

Figure 1. Resolution study for run4. The inclination of the disc relative to the binary as a function of time for the high-mass simulation with $M_d = 0.05\,M$, initial inclination $i = 60°$, $e_b = 0.5$, $R_{in} = 2\,a_b$, and $R_{out} = 5\,a_b$. The model with the solid line initially has 1×10^6 particles, the dashed line has 3×10^5, and the dotted line has 1×10^5. The inclinations are measured at disc radius $R = 5\,a_b$.

In order to describe the evolution of the system, we compute the inclination of the disc relative to the instantaneous binary angular momentum as

$$i_{bd} = \cos^{-1}(\boldsymbol{l}_b \cdot \boldsymbol{l}_d), \quad (1)$$

where $\boldsymbol{l}_{\rm b} = (l_{x\rm b}, l_{y\rm b}, l_{z\rm b})$ is the unit vector in the direction of the binary angular momentum and $\boldsymbol{l}_{\rm d} = (l_{x\rm d}, l_{y\rm d}, l_{z\rm d})$ is a unit vector in the direction of the disc angular momentum vector. The longitude of ascending node phase angle for the disc is

$$\phi_{\rm d} = \tan^{-1}\left(\frac{l_{y\rm d}}{l_{x\rm d}}\right) + \frac{\pi}{2}. \quad (2)$$

We also determine the phase angle of the eccentricity vector of the binary projected on to the reference plane. We define this phase angle as

$$\phi_{\rm b} = \tan^{-1}\left(\frac{e_{y\rm b}}{e_{x\rm b}}\right) + \frac{\pi}{2}. \quad (3)$$

This phase is plotted as red lines in the figures that we describe later. The inclination of the binary relative to the reference plane varies in time and is defined as

$$i_{\rm b} = \cos^{-1}\left(l_{z\rm b}\right). \quad (4)$$

This angle is plotted as blue lines in the figures that we describe later.

2.2 Effect of the disc mass on the disc alignment

We first consider the effect of the disc mass on the standard disc model parameters shown in run1 of Table 1 that is the same model presented in Martin & Lubow (2017). The binary is equal mass with an initial orbital eccentricity of 0.5. The disc is initially inclined by 60° to the binary orbital plane. We calculate disc properties by dividing the disc into 100 bins in spherical radius. Within each bin, we calculate the mean properties of the particles, such as the surface density, inclination, longitude of ascending node, and eccentricity.

The top left panel of Fig. 2 shows the evolution of the disc with our standard parameters in run1. We plot the evolution at a disc radius of $r = 3\,a_{\rm b}$ (solid lines) and $r = 5\,a_{\rm b}$ (dashed lines). The disc acts like a solid body since these lines nearly overlap. As described in Martin & Lubow (2017), the disc undergoes nodal libration in which the tilt and longitude of the ascending node oscillate. Dissipation causes the disc to evolve towards polar alignment where $i_{\rm bd} \approx 90°$. The disc angular momentum vector aligns with the eccentricity vector of the binary and the disc approaches a non-precessing state. For this low-mass disc, there is little evolution of the binary separation, eccentricity vector (as shown by the red line), or inclination (as shown by the blue line). The top left panel of Fig. 3 shows the disc at a time of $t = 1000\,P_{\rm orb}$. The disc is close to polar alignment with the angular momentum of the disc being close to alignment with the binary eccentricity vector (shown in red).

The other panels in Fig. 2 show the disc evolution with a higher initial mass of $M_{\rm d} = 0.01\,M$ (top right, run2), $M_{\rm d} = 0.02\,M$ (bottom left, run3), and $M_{\rm d} = 0.05\,M$ (bottom right, run4). Now the effect of the disc on the binary is no longer negligible. The binary undergoes apsidal precession (as seen by the red line in the phase angle plot), the binary inclination changes (see the blue lines), and the magnitude of the eccentricity of the binary oscillates and decays.

For all four disc masses in Fig. 2, the binary and disc phase angles are nearly the equal. The phase difference undergoes a small amplitude oscillation. Over this time, the disc is then nodally librating with respect to the binary, rather than circulating. The libration indicates that the system is in a state where it lies above the critical level of misalignment for polar-like behaviour. This suggests that the system is undergoing evolution towards a polar-like state as found in the low-mass disc case. There is a small reduction in binary semimajor axis that becomes larger with disc mass. In addition, the binary eccentricity has declined somewhat after about 1000 binary orbits. The eccentricity oscillates, but the eccentricity decreases overall with disc mass. The reduction of binary eccentricity suggests that over longer time-scales the disc might eventually become coplanar with the binary, since the polar disc mechanism requires a certain level binary eccentricity. Better resolution is required to study the longer term evolution.

Fig. 4 plots the evolution of the ratio of the angular momentum of the disc to that of the binary, $J_{\rm d}/J_{\rm b}$ for four different simulations that all have $M_{\rm d} = 0.05M$, including the case plotted in the lower right panel of Fig. 2 in the solid line. The ratios oscillate in time because the eccentricity of the binary oscillates. In all four cases, the disc angular momentum is quite significant with $J_{\rm d} \gtrsim 0.3 J_{\rm b}$.

Unlike the very low mass disc case, a disc with significant mass evolves towards a highly misaligned non-precessing state relative to the binary that is not perpendicular to the binary orbital plane. We define the stationary inclination angle that the disc is evolving towards as $i_{\rm bd} = i_{\rm s}$ where the disc precession rate relative to the binary vanishes, i.e. the disc phase angle is stationary (denoted by subscript s) relative to the binary phase angle. Only in the massless circumbinary disc case does the disc evolve to exactly polar alignment with $i_{\rm s} = 90°$.

As we discuss in Section 3.2, angle $i_{\rm s}$ decreases with increasing particle angular momentum. Consequently, a narrow ring with the same orbital radius as the particle should also experience a decrease in the $i_{\rm s}$ with increasing ring mass. Similar effects are expected for a disc. For the disc mass of 0.05 M (bottom right panel of Fig. 2), the binary-disc inclination oscillations are damping and the disc is evolving towards $i_{\rm bd} = i_{\rm s} \approx 65°$. Thus, the mass of the disc plays an important role in the stationary orientation of the system. We discuss this further in Section 4. The top right panel of Fig. 3 shows the high-mass disc at a time of $t = 1000\,P_{\rm orb}$. The disc is close to a stationary state in the frame of the binary, the generalized polar state, that has a lower level of misalignment than the low-mass disc (shown in the top left panel).

Fig. 5 shows the surface density and the smoothing length as a function of radius at three different times for run4, the high-mass disc case. The disc is initially truncated at $R = 5\,a$, but spreads outwards during the simulation. The disc is well resolved ($\langle h \rangle / H < 1$) out to $R = 10\,a$ for the duration of the simulation except in regions of very low density, the innermost and outermost parts of the disc.

2.3 Binary orbital evolution

The binary orbital evolution is affected by a disc with significant mass. The evolution of the binary angular momentum is determined by both the accretion of angular momentum from the disc and the gravitational torques from the disc. The former leads to an accretional torque. Due to our limited resolution in the inner gap, the effects of this torque on the binary evolution are somewhat uncertain. The effects of the accretional torque on the binary have been difficult to determine even in 2D simulations (e.g. Muñoz et al. 2019).

The gravitational torque contributions to binary orbit changes involve the interaction of the disc with binary resonances that in turn depend on properties of the binary. In the coplanar binary-disc case for small binary eccentricity, the theory of resonant disc gravitational torques suggests that the binary eccentricity increases due to the dominant effects of a single resonance in the disc (Artymowicz et al. 1991). However, at higher binary eccentricities many resonances can lie within the disc, some of which cause binary

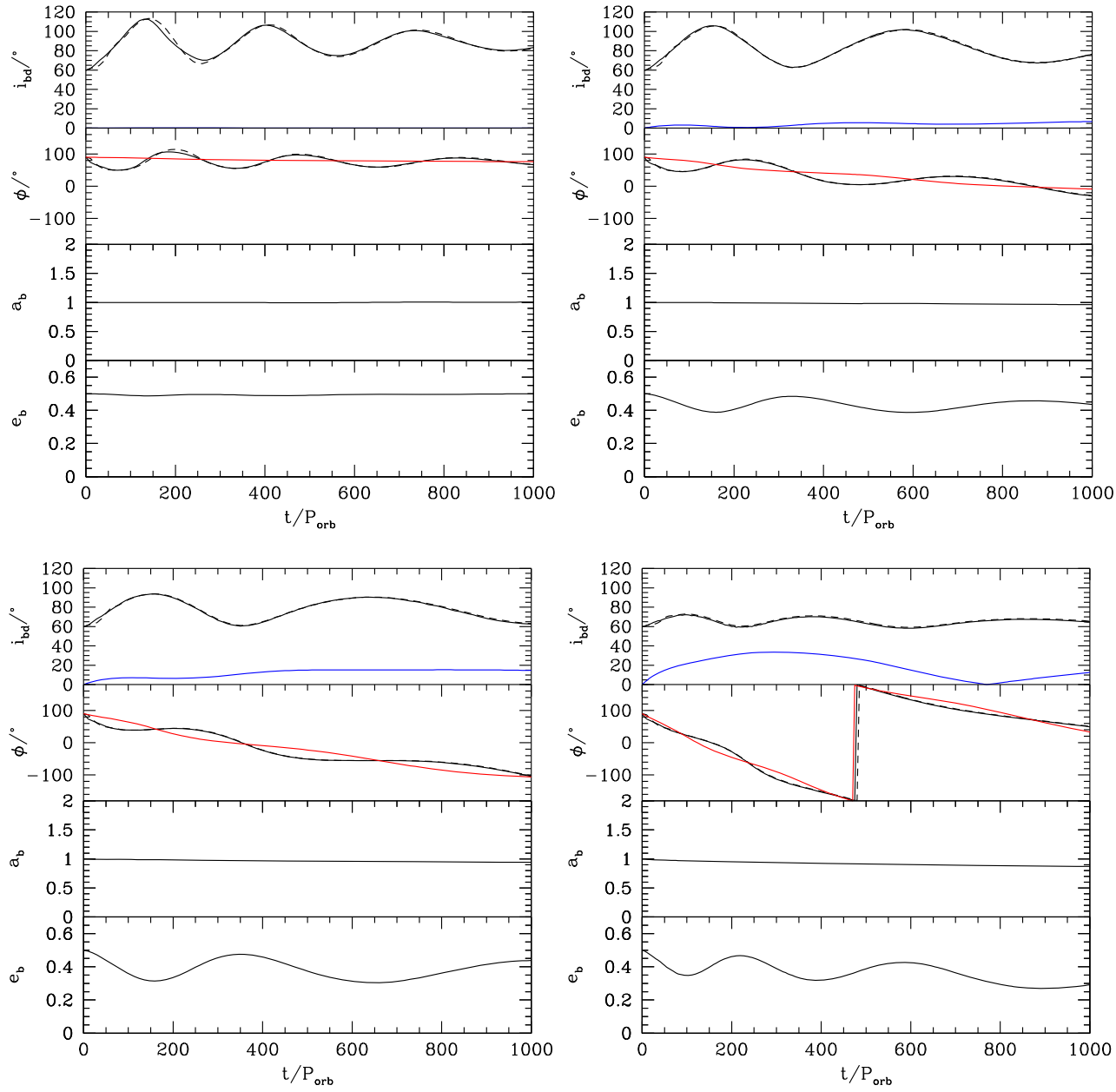

Figure 2. Simulations of a circumbinary disc around an equal mass binary with initial binary eccentricity $e_b = 0.5$, initial disc inclination $i = 60°$, and $H/R = 0.1$ at the disc inner edge of $R_{in} = 2\,a_b$. The disc outer edge is initially at $R_{out} = 5\,a_b$. In the upper two panels, the solid lines are for a radius of $R = 3\,a_b$ and the dashed lines for $R = 5\,a_b$. Top left: $M_d = 0.001\,M$ (run1). Top right: $M_d = 0.01\,M$ (run2). Bottom left: $M_d = 0.02\,M$ (run3). Bottom right: $M_d = 0.05\,M$ (run4). Upper panels: Inclination of the disc angular momentum vector relative to the binary angular momentum vector, i_{bd} (equation 1). The blue lines plot the inclination of angular momentum vector of the binary relative to the reference plane, i_b (equation 4). Second panels: Precession angles ϕ. The black lines show the nodal precession angle for the disc ϕ_d (equation 2). The red lines show the binary eccentricity vector phase angle ϕ_b (equation 3). Third panels: Semimajor axis of the binary a_b. Lower panels: Magnitude of the eccentricity of the binary, e_b.

eccentricity damping. For eccentricities $e_b \sim 0.5$ or greater, the binary eccentricity growth rate due to disc resonances may become very small or even become negative (Lubow & Artymowicz 1992).

Simulations by Artymowicz et al. (1991) found that for an initially low eccentricity binary, $e_b = 0.1$, the eccentricity of the binary increased due to gravitational interactions with the disc. Armitage & Natarajan (2005) confirmed this increase in eccentricity along with a decreasing semimajor axis and suggested that this may solve the final parsec problem of merging massive black hole binaries, at least for extreme mass ratio binaries. More recently, Shi et al. (2012) performed the first 3D magnetohydrodynamic (MHD) simulations of a circumbinary disc around an equal mass circular binary. They found that the MHD stresses allowed accretion on to the binary resulting in the semimajor axis increasing slowly. Miranda, Muñoz & Lai (2017) and Muñoz et al. (2019) performed hydrodynamical simulations with a grid code for a range of binary eccentricities and found that the binary separation increases in time.

Because of the sensitivity of the binary evolution to system parameters, we consider here for comparison the evolution in our

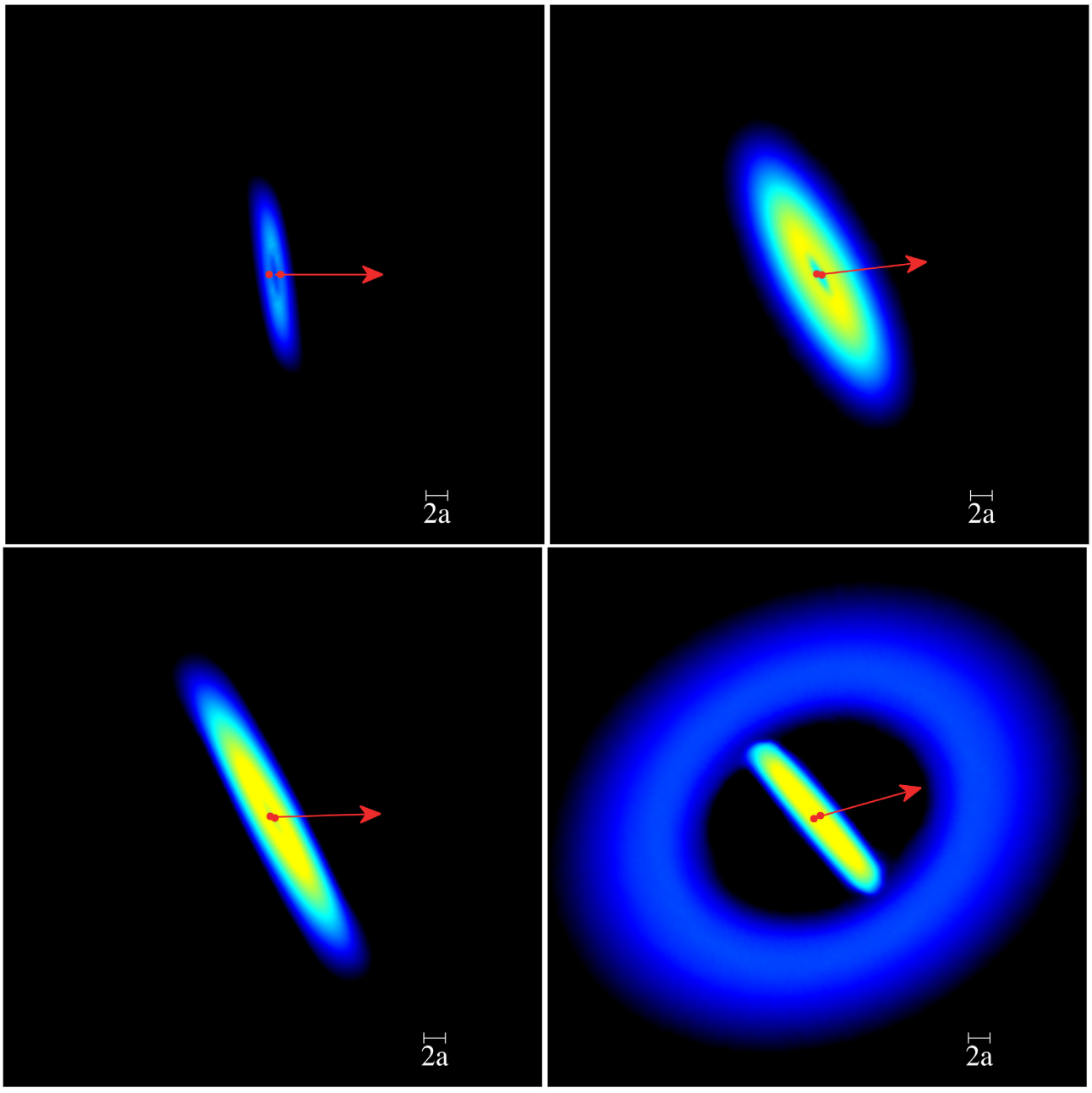

Figure 3. Circumbinary disc around an equal mass binary with initial binary eccentricity $e_b = 0.5$, initial disc inclination $i = 60^\circ$ and $H/R = 0.1$ at the initial disc inner edge of $R_{in} = 2\,a_b$. The system is shown at a time of $t = 1000\,P_{orb}$. Top left: The low-mass narrow disc case $M_d = 0.001\,M$ and $R_{out} = 5\,a_b$ (run1). Top right: The high-mass narrow disc with $M_d = 0.05\,M$ and $R_{out} = 5\,a_b$ (run4). Bottom left: The extended disc with $M_d = 0.05\,M$ and $R_{out} = 10\,a_b$ (run20). Bottom right: The extended disc with $M_d = 0.05\,M$ and $R_{out} = 20\,a_b$ (run21). The z-axis corresponds to the initial binary angular momentum vector. The viewing angle is rotated about the z-axis so that the binary eccentricity vector lies in the plane of the figure and its direction is shown by the red arrow. The red circles show the binary components. The colour denotes the gas density with yellow being about three orders of magnitude higher than blue.

SPH models in the coplanar case. The black lines in Fig. 6 show the evolution of the binary in three coplanar disc simulations for varying disc mass. The eccentricity of the binary decreases in time while the semimajor axis also decreases. The eccentricity change is somewhat insensitive to the mass of the disc while the semimajor axis decreases more quickly for larger disc mass. For comparison, in the blue lines in Fig. 6 we also show the binary orbit evolution in our standard inclination parameters of run1 and the high-mass disc of run4. A low-mass inclined disc leads to very little binary orbital evolution over the time-scale of our simulation. The higher mass disc leads to more binary eccentricity evolution, as we discussed in the previous subsection.

2.4 Critical inclination for circulating and librating solutions

There is a critical inclination above which the disc is librating and below which it circulates. In Lubow & Martin (2018), we found that for a low-mass disc, the critical inclination is close to that predicted for a test particle orbit. As we discuss in Section 3.3, the critical inclination for a third body with non-zero mass depends

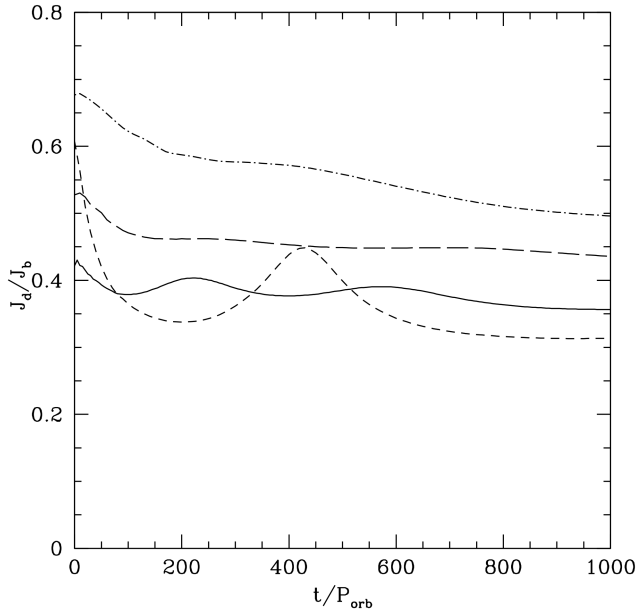

Figure 4. The evolution of the ratio of the angular momentum of the disc to the angular momentum of the binary for run4 (solid line), run14 (short-dashed line), run20 (long-dashed line), and run21 (dot–dashed line).

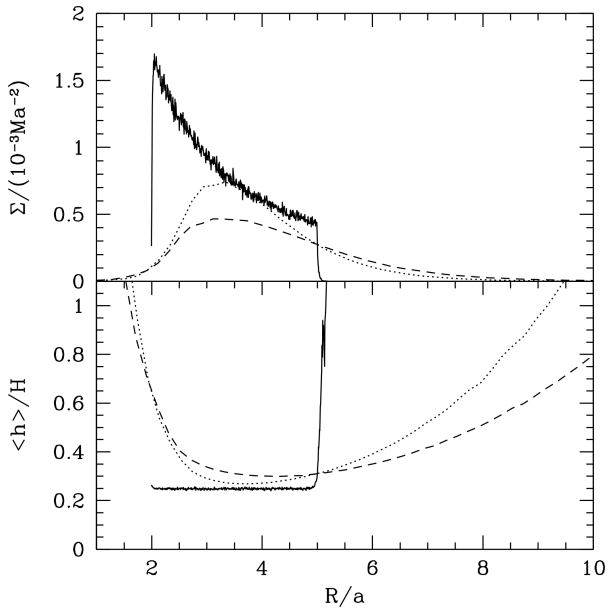

Figure 5. The surface density (upper) and smoothing length-to-disc scale height ratio (lower) as a function of radius in the disc for run4 at times $t =$ 0 (solid lines), 500 (dotted lines), and 1000 P_{orb} (dashed lines).

upon the angular momentum of the body. Here, we consider the critical inclination for two different binary eccentricities.

2.4.1 *Initial binary eccentricity* e = *0.5*

Fig. 7 shows the effect of changing the initial inclination of the disc for an initially high disc mass of 0.05 M and an initial binary eccentricity of 0.5. The simulations that have initial inclination 20° (top left, run8), 40° (top right, run9), and 50° (bottom left, run10) undergo nodal phase circulation of the disc relative to the binary. The

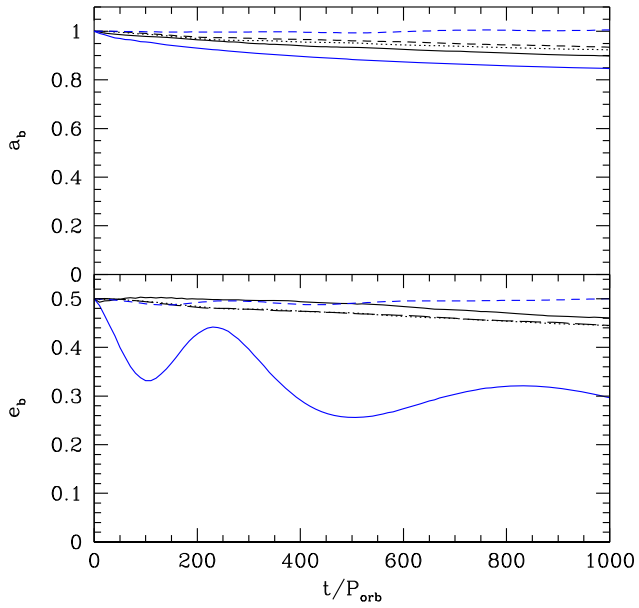

Figure 6. The binary semimajor axis and eccentricity evolution due to a coplanar circumbinary disc. The initial disc mass is 0.05 M (solid black lines, run5), 0.01 M (dotted black lines, run6), and 0.001 M (dashed black lines, run7) and otherwise the same initial disc properties. The blue lines show for comparison the standard parameters with a disc mass of 0.001 M and an inclination of 60° (dashed blue lines, run1) and a disc mass of 0.05 M and an inclination of 60° (solid blue lines, run4).

disc and the binary are seen to be precessing in opposite directions. However, for initial inclination of 60° (bottom right of Fig. 2, run4) and 80° (bottom right of Fig. 7, run11), the disc is librating relative to the binary. The precession angles of the binary and the disc are nearly locked together. Thus, the critical angle between the two types of solution for these parameters is in the range 50−60°. A disc in this librating state is then in a polar-like orbit around the binary.

For the disc with the initial inclination of 80°, the tilt oscillations are in the opposite direction to the lower inclination discs. In other words, the inclination initially decreases and the eccentricity increases, vice versa for the lower inclination simulations. The disc is approaching its generalized polar angle i_s from above.

2.4.2 *Binary eccentricity* e = *0.8*

Fig. 8 shows the effect of changing the inclination of the disc around a binary with a higher eccentricity of $e_b = 0.8$. The disc varies from circulating phase at initial inclination of 20° (top left panel, run12) to librating phase for initial inclination 40° (top right panel, run14). Although we do not show a figure, we also ran a simulation with an initial inclination of 30° and find that it is circulating (see run13 in Table 1). Thus, the critical angle is between 20 and 30°. This angle is higher than the critical angle expected for a test particle of 16° based on equation 2 of Doolin & Blundell (2011). The angular momentum evolution of the simulation that begins at 40° (run14) is shown in the short-dashed line in Fig. 4.

2.5 Size of the disc

The size of the disc relative to the binary separation may take a wide range of values. Protoplanetary discs are thought to extend to

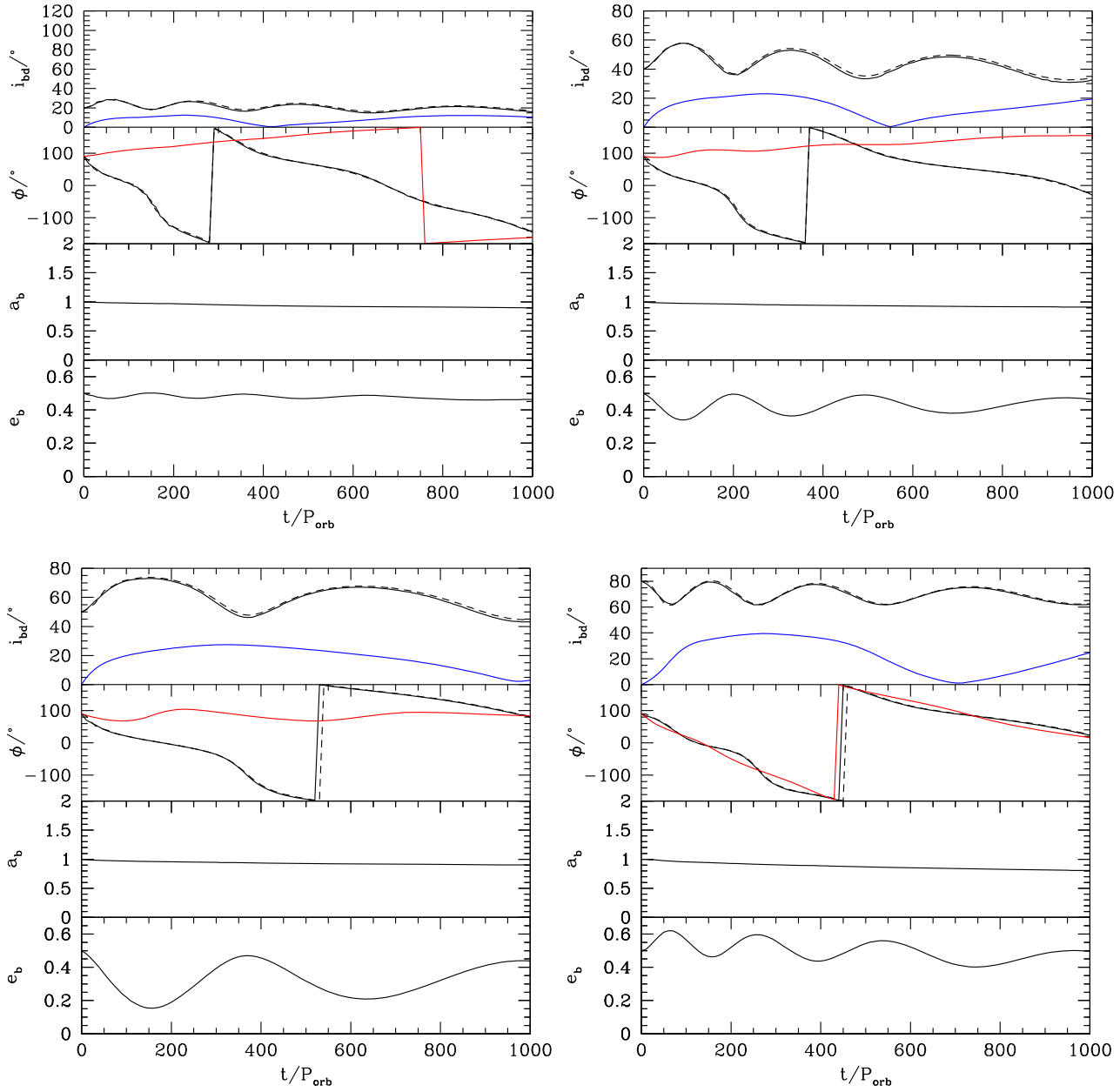

Figure 7. The effect of the initial inclination on the evolution of the high-mass disc with initial mass $M_d = 0.05\,M$ and $e_b = 0.5$ initially. Top left: Initial inclination of 20° (run8). Top right: Initial inclination of 40° (run9). Bottom left: Initial inclination of 50° (run10). Bottom right: Initial inclination of 80° (run11).

around hundreds of au (e.g. Williams & Cieza 2011). For a close binary, this may be several hundred binary separations. However, for a wider binary this may be only a few times the binary separation. The simulations we have considered so far in this work have a moderate extent and are relevant to wider binaries. In Martin & Lubow (2018) we found that extending the outer disc radius, relative to the binary separation led to warped and even broken discs. If the sound crossing time-scale over the disc is longer than the precession time-scale, then the disc is unable to communicate fast enough to remain as a solid body.

2.5.1 *Initial disc outer radius* $R = 10\,a_b$

Fig. 9 shows the effect of increasing the initial size of the disc to $10\,a_b$ compared to $5\,a_b$ that we previously described. The figure shows the same four disc masses as shown in Fig. 2. The qualitative behaviour of the disc has not changed by increasing the initial disc radius. In each case, the disc is in a librating state. The two lines in the inclination and phase angle plots show the disc at a radius of $3\,a_b$ (solid lines) and $10\,a_b$ (dashed lines). There is a much more noticeable difference between these two radii now. That is, there is more warping in the larger disc. The warping is larger for the smaller disc mass because the tilt oscillations are larger. For high-mass broader disc, the generalized polar (stationary) inclination is $i_s \approx 60°$ that is slightly lower than for the narrower disc. Thus, the disc begins very close to its stationary angle i_s and so there is little inclination evolution. For the largest disc mass considered (run20), the evolution of the ratio of the disc angular momentum to the binary angular momentum is shown in the long-dashed line in

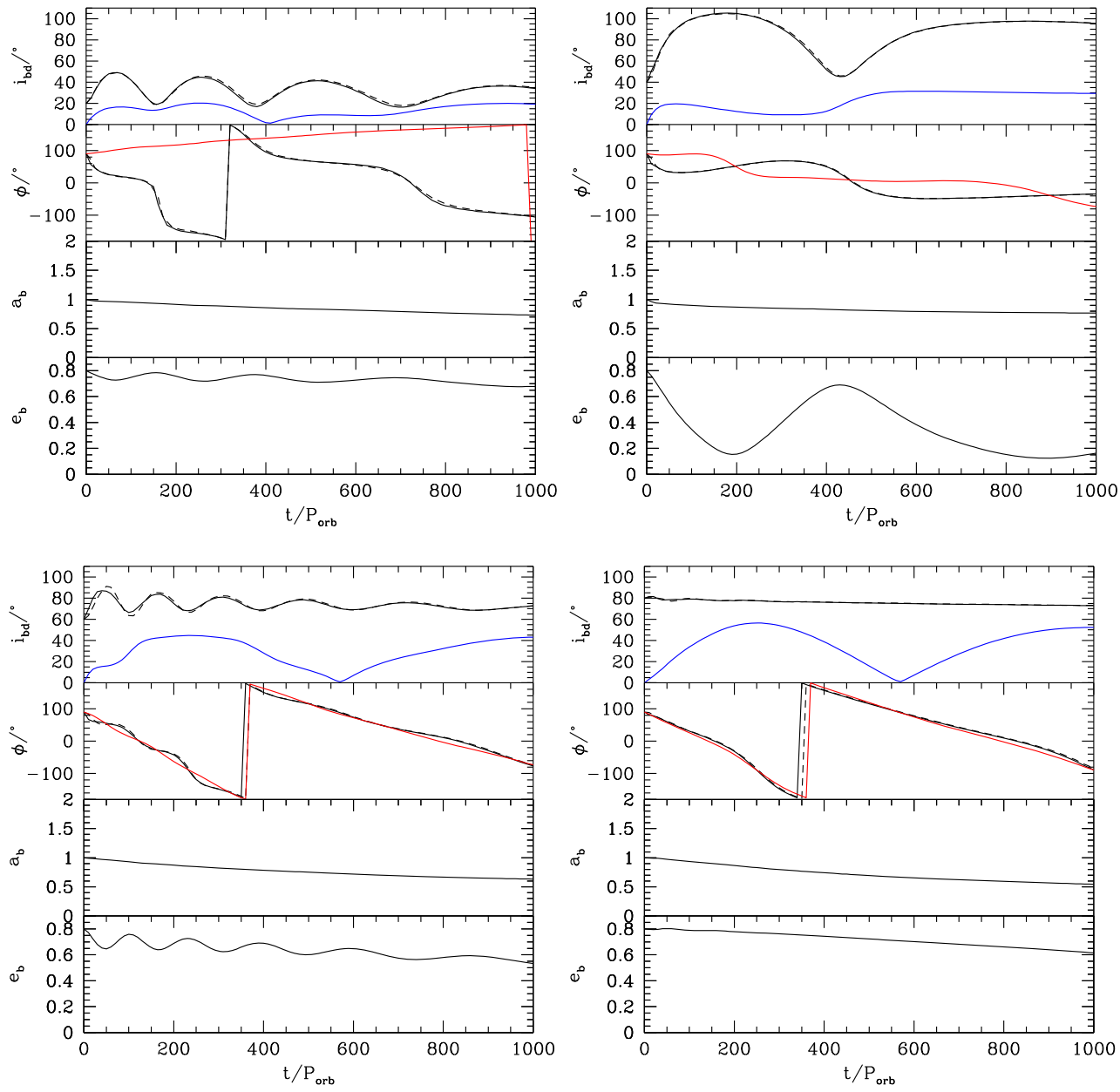

Figure 8. The effect of the initial inclination on the evolution of the high-mass disc with initial mass $M_{\rm d} = 0.05\,M$ and $e_{\rm b} = 0.8$. Top left: Initial inclination of 20° (run12). Top right: Initial inclination of 40° (run14). Bottom left: Initial inclination of 50° (run15). Bottom right: Initial inclination of 80° (run16).

Fig. 4. The lower left panel of Fig. 3 shows the disc at a time of $t = 1000\,P_{\rm orb}$.

2.5.2 *Initial disc outer radius* $R = 20\,a_{\rm b}$

The left-hand panel of Fig. 10 shows the high disc initial mass case of $M_{\rm d} = 0.05\,M$ with an even larger initial disc outer radius of $20\,a_{\rm b}$ (run21). The two lines in the inclination and phase angle plots show the disc conditions at a radius of $3\,a_{\rm b}$ (solid lines) and $20\,a_{\rm b}$ (dashed lines). There is significant difference in properties between the two parts of the disc. Hence in the right-hand panel we show the surface density, inclination and phase angle as a function of radius at three different times. There is a clear break in the disc at a radius of about $10\,a_{\rm b}$. Circumbinary discs simulations around circular binaries have previously shown this behaviour (Nixon et al. 2012; Nixon & King 2012). The inner and the outer parts of the disc precess independently and show tilt oscillations on different time-scales. The inner part of the broken disc at least can still achieve polar alignment. For this simulation (run21), the evolution of the ratio of the disc angular momentum to the binary angular momentum is shown in the dot–dashed line in Fig. 4.

The lower right panel of Fig. 3 shows the broken disc at a time of $t = 1000\,P_{\rm orb}$. The inner part of the disc is in a generalized polar aligned state while the outer part remains misaligned. The lower panel on the right-hand side of Fig. 10 shows the smoothing length as a function of radius in the breaking disc. At the break, the

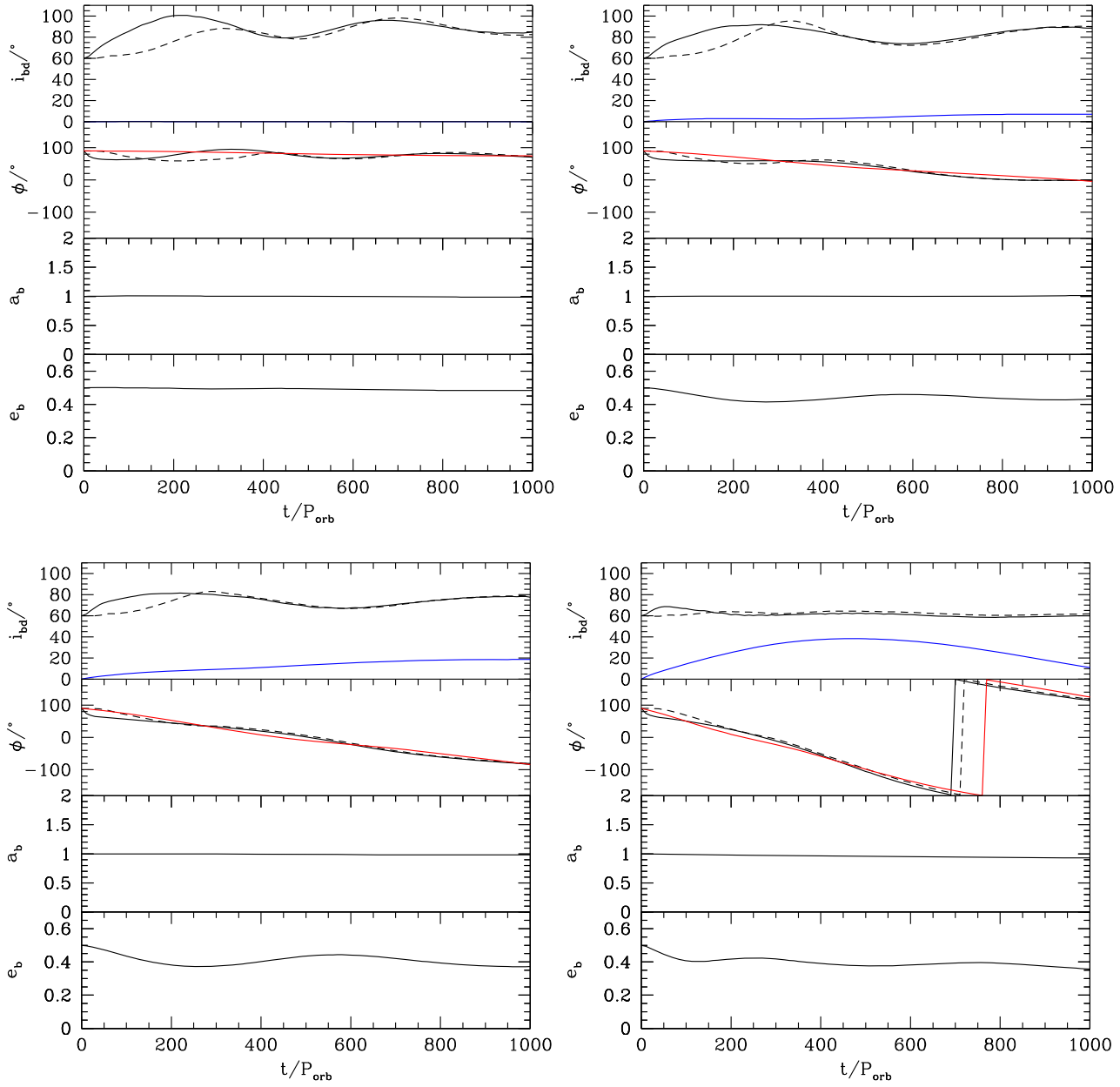

Figure 9. Same as Fig. 2 except the initial disc outer radius is $10\,a_{\rm b}$. The initial mass of the disc is 0.001 M (top left, run17), 0.01 M (top right, run18), 0.02 M (bottom left, run19), and 0.05 M (bottom right, run20). The solid lines show a radius of $R = 3\,a_{\rm b}$ and the dashed lines $R = 10\,a_{\rm b}$.

smoothing length increases because of the small amount of material in the low-density gap (see Fig. 3). Disc breaking, as we find, can only be seen in discs with sufficiently high resolution (Nealon, Price & Nixon 2015).

3 GENERALIZED POLAR ALIGNMENT OF A RING WITH MASS

The secular dynamics of a circumbinary particle are identical to those of a narrow circumbinary ring. In order to understand the stable polar alignment of a disc with significant mass, in this section we consider a three-body problem for a circumbinary particle that takes into account the gravitational effects of the masses of all three bodies. We first determine the inclination at the centre of the librating region $i_{\rm s}$, where the ring (particle) nodal phase is stationary with respect to the binary nodal phase. We then determine the conditions required for a circumbinary ring to evolve into a stationary (polar) configuration. The ring model provides insight into the effects gravitational interactions by the orbiting ring. But it does not include possible effects due to the radial extension of a disc or the advection of disc mass and angular momentum on to the binary.

3.1 Evolution equations

Farago & Laskar (2010) developed a secular theory for the motion of a circumbinary particle of non-zero mass. The principal approximation is that the binary potential is calculated in the quadrupole

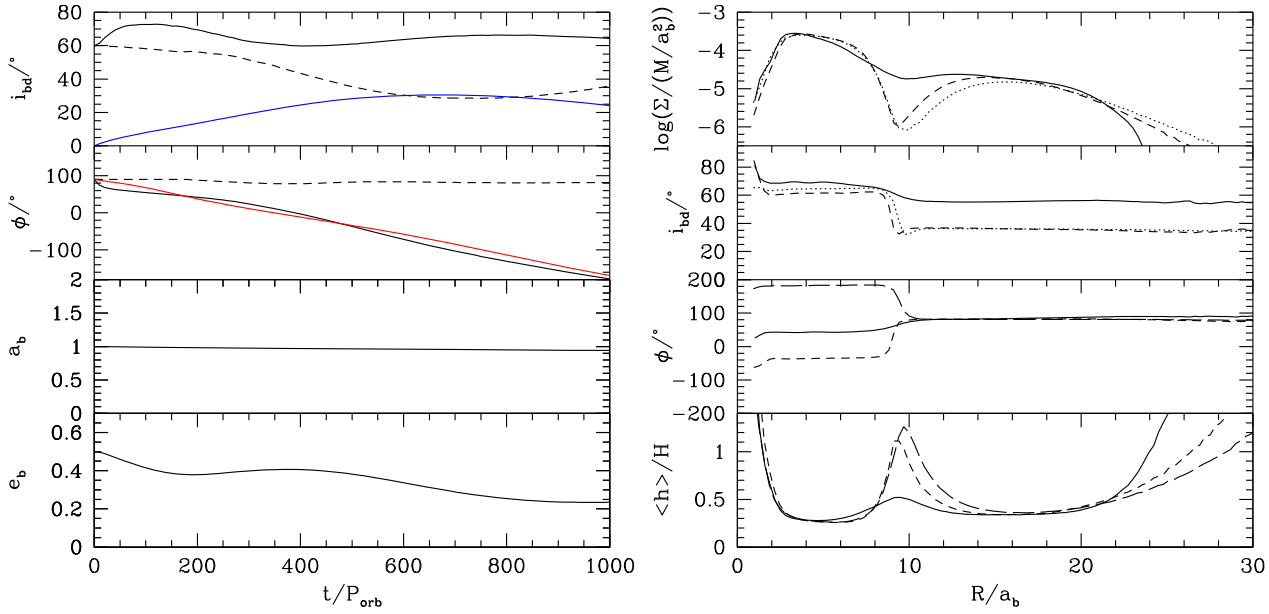

Figure 10. Left: Same as the lower right panel of Fig. 2 except the initial disc outer radius is $20\,a_{\rm b}$. The initial mass of the disc is $0.05\,M$ (run21). The solid lines show a radius of $R = 3\,a_{\rm b}$ and the dashed lines $R = 20\,a_{\rm b}$. Right: The surface density, inclination, phase angle, and smoothing length-to-disc scale height ratio as a function of radius at times $t = 200\,P_{\rm orb}$ (solid lines), $t = 500\,P_{\rm orb}$ (dashed lines), and $t = 1000\,P_{\rm orb}$ (dotted lines).

approximation. They utilize a Cartesian coordinate system that is defined relative to the binary orbit. The orbit changes in time due to gravitational interactions with the particle. The x-direction is along the instantaneous eccentricity vector of the binary, the z-direction is along the instantaneous binary angular momentum, and the y-direction is orthogonal to the x- and z-directions. The origin lies at the instantaneous centre of mass of the binary. The equations of motion of the particle are expressed in terms of a unit vector that lies along the direction of the ring's (particle's) angular momentum that we denote by tilt vector $\boldsymbol{\ell} = (\ell_x, \ell_y, \ell_z)$ in this coordinate system.

As shown by Farago & Laskar (2010), the circumbinary ring semimajor axis, the eccentricity (that we assume to be zero), and its angular momentum, $J_{\rm r}$, are constants of motion. For the binary, the semimajor axis $a_{\rm b}$ is a constant of motion, while its eccentricity, angular momentum $J_{\rm b}$, and binary-ring mutual inclination i are not constants of motion. However, the system angular momentum J is a constant of motion. These properties imply that

$$J_{\rm b}^2 + 2J_{\rm b}J_{\rm r}\cos i = J^2 - J_{\rm r}^2, \tag{5}$$

where the LHS is a constant of motion. In this equation, since $a_{\rm b}$ is a constant of motion, binary angular momentum $J_{\rm b}$ varies in time due to variations in binary eccentricity $e_{\rm b}$ as inclination i varies in time. This equation then determines a relationship between $e_{\rm b}$ and i. In the limit that $J_{\rm b} \gg J_{\rm r}$, equation (5) implies that $J_{\rm b}$ and therefore $e_{\rm b}$ are constants of motion, as applies for a low-mass ring. In the opposite limit of a very massive ring $J_{\rm b} \ll J_{\rm r}$, we have that $J_{\rm b}\cos i$ is a constant of motion. This condition holds because the z component of the binary angular momentum is conserved due to the static potential imposed by the massive stationary ring. The constant of motion in this case plays a key role in the study of Kozai–Lidov oscillations (Kozai 1962; Lidov 1962).

The equations of motion track the variations in time of the tilt vector $\boldsymbol{\ell}$ and the binary eccentricity $e_{\rm b}$. We apply the secular evolution equations 3.15–3.18 of Farago & Laskar (2010). We make some changes in variables. We also make use of the ratio of the ring-to-binary angular momentum

$$j = \frac{J_{\rm r}}{J_{\rm b}}. \tag{6}$$

The angular momentum ratio j generally varies in time because $J_{\rm b}$ varies in time, while $J_{\rm r}$ does not change in time. We write the evolution equations as

$$\frac{{\rm d}\ell_x}{{\rm d}\tau} = \left(1-e_{\rm b}^2\right)\ell_y\ell_z + \gamma_{\rm r}\sqrt{1-e_{\rm b}^2}\,\ell_y\left(2-5\ell_x^2\right), \tag{7}$$

$$\frac{{\rm d}\ell_y}{{\rm d}\tau} = -\left(1+4e_{\rm b}^2\right)\ell_x\ell_z - \frac{\gamma_{\rm r}\ell_x}{\sqrt{1-e_{\rm b}^2}}\left(\left(1-e_{\rm b}^2\right)\left(2-5\ell_x^2\right)+5e_{\rm b}^2\ell_z^2\right), \tag{8}$$

$$\frac{{\rm d}\ell_z}{{\rm d}\tau} = 5e_{\rm b}^2\ell_x\ell_y + \frac{5\gamma_{\rm r}e_{\rm b}^2}{\sqrt{1-e_{\rm b}^2}}\ell_x\ell_y\ell_z, \tag{9}$$

$$\frac{{\rm d}e_{\rm b}}{{\rm d}\tau} = 5\gamma_{\rm r}e_{\rm b}\sqrt{1-e_{\rm b}^2}\ell_x\ell_y, \tag{10}$$

where we apply a scaled time equal to $\tau = \alpha' t$ for time t in taking the time derivatives above. Quantity α' is constant in time and is defined by equation 3.9 of Farago & Laskar (2010). For our purposes of determining closed orbits, we do not care about the actual time t and therefore do not need to know the value of α'. So we use τ as our time coordinate. Quantity $\gamma_{\rm r}$ is proportional to the ring angular momentum and is a constant of motion

$$\gamma_{\rm r} = \sqrt{1-e_{\rm b}^2}\,j. \tag{11}$$

For the purposes of numerically integrating these equations, it is convenient to set $\gamma_{\rm r}$ as

$$\gamma_{\rm r} = \sqrt{1-e_{\rm b0}^2}\,j_0, \tag{12}$$

where e_{b0} and j_0 are the initial eccentricity and ring-to-binary angular momentum ratio, respectively.

3.2 Stationary inclination

We are interested in determining the conditions for $\boldsymbol{\ell}$ to be stationary in the $\ell_y = 0$ plane. We then require that

$$\frac{d\boldsymbol{\ell}}{d\tau} = 0, \tag{13}$$

$$\frac{de_b}{d\tau} = 0 \tag{14}$$

in equations (7)–(10). For the test particle case, we know that this occurs when the particle orbit lies perpendicular to the binary orbital plane so that $\boldsymbol{\ell} = (1, 0, 0)$. (It also occurs for $\boldsymbol{\ell} = (-1, 0, 0)$ corresponding to an anti-alignment of particle angular momentum with binary eccentricity. But we omit discussion of that orientation.) In the present case, we take into account the non-zero ring mass. The stationary condition in the $\ell_y = 0$ plane is given by

$$\ell_x = \sqrt{1 - \ell_z^2}, \tag{15}$$

$$\ell_y = 0, \tag{16}$$

$$\ell_z = \frac{-\left(1 + 4e_b^2\right) + \sqrt{\left(1 + 4e_b^2\right)^2 + 60\left(1 - e_b^2\right) j^2}}{10\, j}, \tag{17}$$

as is consistent with appendix A.4 of Farago & Laskar (2010) (see Appendix A). In this stationary state, the binary eccentricity $e_b = e_{b0}$ and the ring-to-binary angular momentum ratio $j = j_0$ are constant in time. From equation (17), we can obtain the stationary tilt angle of the ring relative to the binary using the fact that

$$\cos i_s = \ell_z. \tag{18}$$

For small ring angular momentum, $j \ll 1$, we have that

$$\cos i_s \simeq \frac{3j\,\left(1 - e_b^2\right)}{1 + 4e_b^2}. \tag{19}$$

A zero mass stationary ring is then perpendicular to the binary orbital plane, as expected. For arbitrary ring mass, in the limit of high eccentricity close to unity, we have that

$$\cos i_s \simeq \frac{6j\,(1 - e_b)}{5}. \tag{20}$$

The stationary tilt angle i_s then increases with binary eccentricity. The stationary angle is achieved at a near perpendicular orientation for sufficiently large binary eccentricity. In the limit of large ring angular momentum $j \gg 1$, the stationary inclination is

$$\cos i_s \simeq \sqrt{\frac{3}{5}\left(1 - e_b^2\right)}. \tag{21}$$

Note that in the case of circular binary orbit, the stationary angle is the critical angle for Kozai–Lidov oscillations of 39.2° (Kozai 1962; Lidov 1962).

Fig. 11 shows the stationary inclination as a function of the ratio of the ring angular momentum to the binary angular momentum for three different binary eccentricities (using equations 17 and 18). The dashed lines show the corresponding limit of large particle angular momentum given in equation (21). With increasing ring angular momentum and all other parameters fixed, the stationary tilt angle *decreases monotonically* to the value in the corresponding dashed line given by equation (21) at large J_r/J_b. Zanazzi & Lai (2018) also found that the stationary tilt (fixed point) is less than 90° for a circumbinary particle (ring) with non-zero angular momentum. They obtained numerical results for this problem with different conditions for stationary solutions than our conditions given by equations (13) and (14). Consequently, our analytical solution (equations 17 and 18) does not agree with their results plotted in their fig. 7. We compare our analytical stationary inclination to the numerical hydrodynamical disc simulations in Section 3.4.1.

If the binary mass ratio decreases (keeping everything else fixed), the angular momentum of the ring compared to the binary is larger, and therefore j increases. According to equations (17) and (18), this leads to a lower stationary inclination as seen in Fig. 11. As noted in Martin & Lubow (2018), the libration period also increases with the decreasing binary mass ratio. Thus, the time-scale to reach the generalized polar state is also affected by the binary mass ratio.

3.3 Conditions for polar evolution

We consider here the conditions required for a ring with non-zero mass to evolve towards a stationary non-coplanar (polar) orientation. For such evolution to occur, the ring needs to be in a state where its angular momentum direction $\boldsymbol{l}$ undergoes libration oscillations about the stationary direction described in Section 3.2.

We determine the minimum inclination required for a librating orbit, given the binary eccentricity and a measure of the ring-to-binary angular momentum j. Since this ratio varies in time as J_b varies, we select a value of $j = j_0$ where the line of ascending notes is equal to $\phi = 90°$ and the inclination is smaller than the stationary value i_s. The latter condition is applied because a librating orbit of $\boldsymbol{l}$ forms a closed loop that is double valued in ϕ corresponding to two different values of inclination i (see points A and C in Fig. 12). We select the j value at the smaller value of i ($i < i_s$) for the reference quantity j_0. Similarly binary eccentricity e_b varies in time and we apply the value of the reference binary eccentricity e_{b0} that is the value of eccentricity at this same phase $\phi = 90°$ and inclination.

For a given initial value of binary eccentricity e_{b0}, angular momentum ratio j_0, and assumed initial binary-ring inclination $i_0 < i_s$, we integrate the evolution equations (7)–(10) together with equation (12). The initial conditions are given by

$$(\ell_x, \ell_y, \ell_z, e_b) = (\sin i_0, 0, \cos i_0, e_{b0}). \tag{22}$$

For a fixed set of values of e_{b0} and j_0, we determine the minimum value of i_0 for which the orbit of $\boldsymbol{\ell}$ is librating, rather than circulating. This is done using a bisection method. We sometimes refer to that librating orbit as the critical orbit.

Fig. 12 plots two critical librating orbits as heavy black lines in a phase portrait of $i\cos\phi$ versus $i\sin\phi$. The distance from the origin to a point on the plot is the mutual inclination i, while the angle from horizontal to the line from the origin to a point on the plot is equal to the longitude of ascending node ϕ. Both plots are for a system with $e_{b0} = 0.5$. The upper plot has $j_0 = 0.1$, while the lower plot has $j_0 = 0.3$. The grey lines plot the circulating orbits that result from slightly smaller values of i_0 than for the critical orbit. Both the minimum and maximum values of i along an orbit always occur where $\phi = 90°$ corresponding to points A and C in Fig. 12. The minimum inclination along a librating orbit thus occurs at the initial time when $i = i_0$ (as described above in equation 22).

Fig. 13 plots as a dotted line the numerically determined minimum tilt angles for critical librating orbits as a function of j_0 for

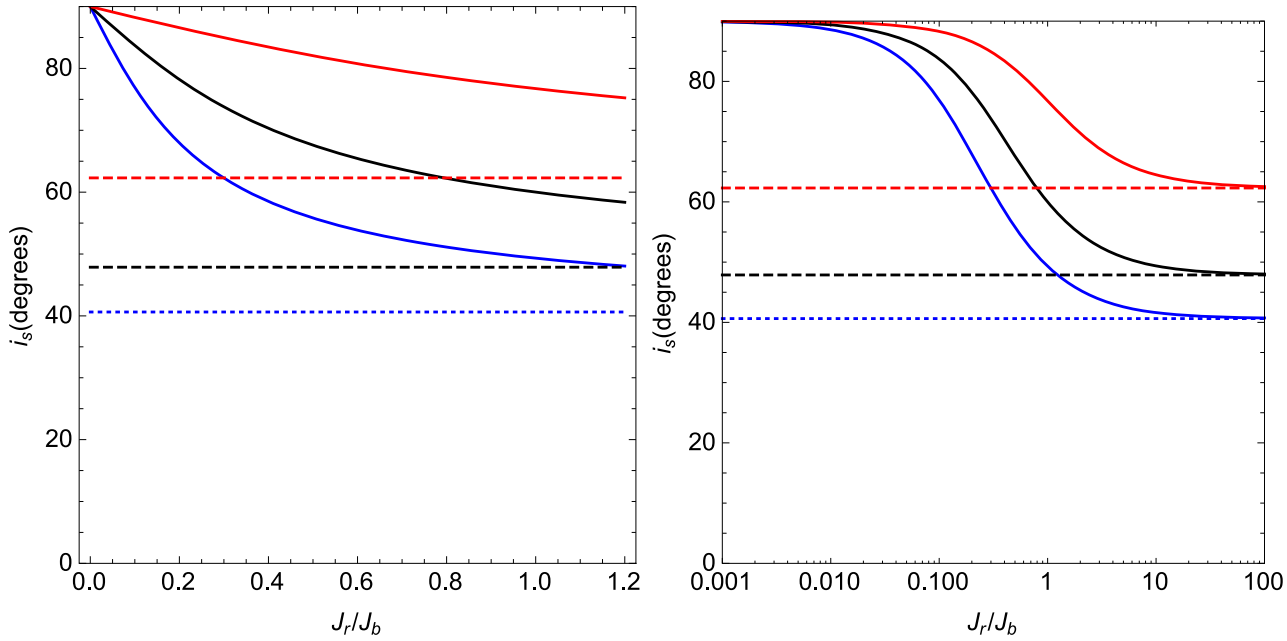

Figure 11. The solid lines show the stationary inclination, i_s, as a function of the ratio of the ring angular momentum to the binary angular momentum for binary eccentricity $e_b = 0.2$ (blue), $e_b = 0.5$ (black), and $e_b = 0.8$ (red) found with equations (17) and (18). The dashed lines show the stationary inclination in the limit that this angular momentum ratio goes to infinity, given by equation (21). The left- and right-hand panels are the same except the right-hand panel is on a log scale to show the convergence to the dashed lines at large J_r.

three different values of binary eccentricity e_{b0}. In addition, the solid blue line plots the stationary angle. Notice that the stationary angles lie above the minimum tilt angles, as expected (point D in Fig. 12 lies above point A). The minimum tilt angle increases with j_0 for small values j_0. It flattens and then decreases for larger values for j_0. If a ring tilt lies above the minimum value given in Fig. 13, it does not immediately follow that the ring is in a librating state. The full condition also involves the phase ϕ as we see below. The condition on tilt is necessary for libration, but not sufficient.

3.3.1 *Lower j/higher* e_b *branch*

For sufficiently small values of j or large values of e_b, it is possible to determine the libration conditions analytically. As seen in the upper panel of Fig. 12 for j small, the critical orbit of $\boldsymbol{\ell}$ that separates libration from circulation has a cusp at $\phi = 0^\circ$ and 180° that corresponds to $\ell_x = 0$ (see points $B_\pm$). The cusp involves $d\boldsymbol{\ell}/d\tau = 0$ on the $\ell_x = 0$ plane (see also appendix A3 of Farago & Laskar 2010). Strictly speaking this is a stationary point. But, this stationary point is unstable, unlike the stationary point in the $\ell_y = 0$ plane corresponding to polar configuration discussed in Section 3.2. Since it is unstable, orbits that lie extremely close to it will diverge away from it, either as a librating or circulating orbit. The librating orbit that comes infinitesimally close to a stationary point with the same binary eccentricity is the critical librating orbit.

From equation (7), we have that this $\ell_x = 0$ stationary point satisfies

$$\ell_{zs} = -\frac{2\gamma_r}{\sqrt{1-e_{bs}^2}} \tag{23}$$

at this stationary point s. From equations (5) and (11), we have that total angular momentum conservation implies

$$\gamma^2 = \gamma_r^2 + 1 - e_b^2 + 2\gamma_r\sqrt{1-e_b^2}\ell_z, \tag{24}$$

where

$$\gamma = \frac{\sqrt{1-e_b^2}\,J_r}{J_b}. \tag{25}$$

Both γ_r and γ are constants of motion. The reason is that the magnitude of the binary angular momentum varies in time due to the variations in its eccentricity only. The quantity $\sqrt{1-e_b^2}/J_b$ is then independent of time. We want to express $\boldsymbol{\ell}$ and e_b at this stationary point as a function of these constants of motion. The reason is that they can then be determined from the values of $\boldsymbol{\ell}$ and e_b at any point along the critical librating orbit. In this way, the value of the Hamiltonian at this stationary point can be determined in terms of these values anywhere along the critical librating orbit by using equations (11) and (24).

By using equation (23) and applying equation (24) to this stationary point, we have that

$$e_{bs} = \sqrt{1-\gamma^2-3\gamma_r^2} \tag{26}$$

and

$$\ell_{zs} = -\frac{2\gamma_r}{\sqrt{\gamma^2+3\gamma_r^2}}, \tag{27}$$

which are the same as equations A12 and A15 of Farago & Laskar (2010).

We consider a secular Hamiltonian based on equation 3.21 of Farago & Laskar (2010)

$$H = \ell_z^2 + e_b^2\left(2-\ell_z^2-5\ell_x^2\right), \tag{28}$$

where we ignore an overall factor that is independent of $\boldsymbol{\ell}$ and e_b that is irrelevant to our considerations below.

The value of the Hamiltonian at this stationary point in the $\ell_x = 0$ plane based on equations (26) and (27) is equal to

$$H_s = 2\left(1-\gamma^2-\gamma_r^2\right). \tag{29}$$

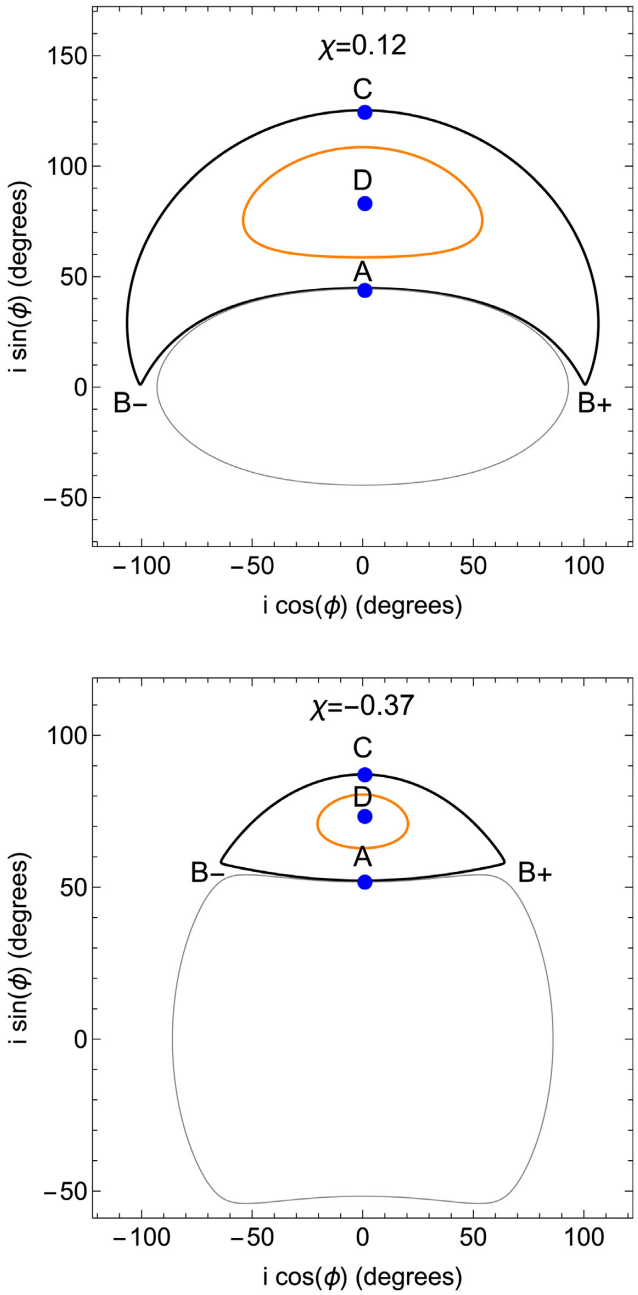

Figure 12. The $i\cos\phi - i\sin\phi$ plane for orbits with varying initial inclinations and all other parameters held fixed. The black curves are the orbits for the minimum angle that produces a librating orbit. The grey curves are for orbits whose inclination is slightly lower and are circulating. Point A on the black line denotes the point that has the minimum angle for a librating orbit. Points $B_{\pm}$ on the black line denotes the location where there is a cusp and the velocity $\mathrm{d}\boldsymbol{l}/\mathrm{d}\tau$ vanishes. Point C on the black line is the location of the maximum tilt angle of a librating orbit. Point D marks the location of the stationary (non-librating) orbit that corresponds to a fixed polar orbit relative to the binary. The orange line plots an intermediate librating orbit. The upper plot has a positive value of χ, while the lower plot has a negative value (see equation 31) that indicates a change in orbit behaviour.

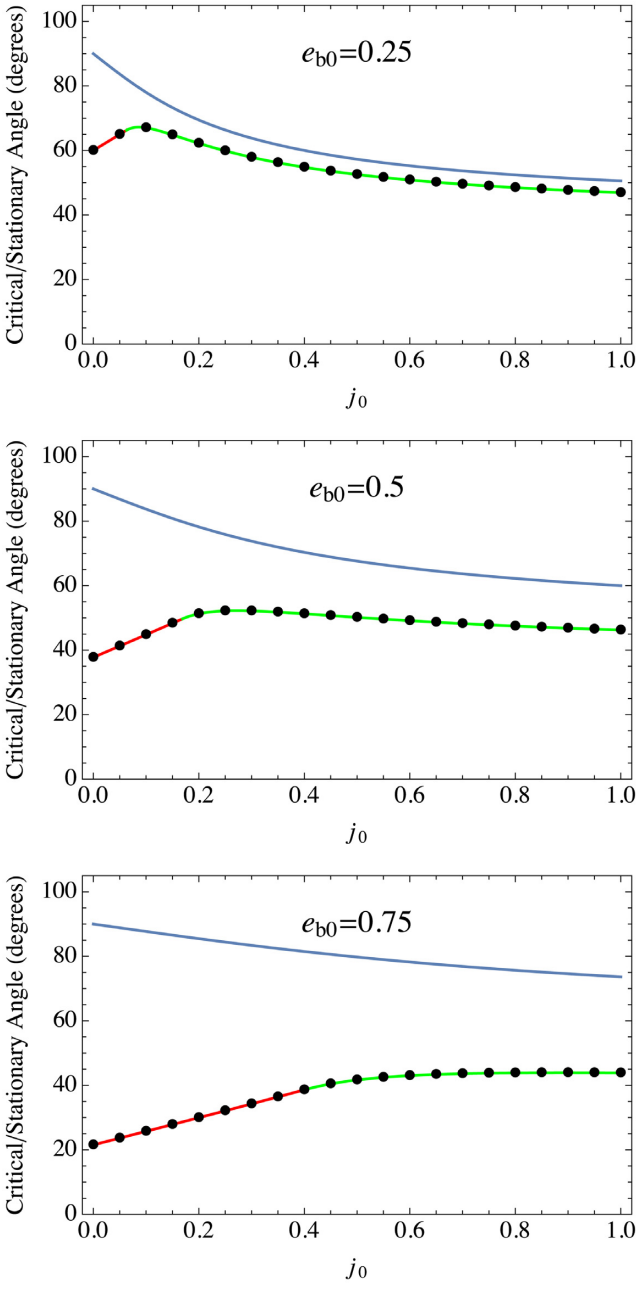

Figure 13. Plots of minimum and stationary tilt angles as a function of the ratio of ring-to-binary angular momentum J_r/J_b at phase $\phi = 90^\circ$ (denoted by j_0) and binary eccentricity at this phase $e_b = e_{b0}$. The dotted lines are the numerically determined minimum tilt angles for libration that leads to generalized polar alignment. The solid blue lines are the tilts for the generalized polar alignment (stationary points given by equations 17 and 18). The solid red lines are an analytical determination of the minimum tilt angle based on equation (33) over a range of J_r/J_b where $\chi > 0$ in equation (31). The solid green lines are an analytical determination of the minimum tilt angle based on equation (39) over a range of J_r/J_b where $\chi < 0$. The red and green lines meet at $\chi = 0$.

By applying equations (11) and (24), we then have that at any point on the critical librating orbit that has a Hamiltonian value infinitesimally close to H_s

$$H_{cr} = 2\left(e_b^2 - 2\left(1 - e_b^2\right) j(j + \cos i)\right), \tag{30}$$

where we use the fact that $\ell_z = \cos i$. But this equation only holds if e_{bs} is real in equation (26), which again through the application of equations (11) and (24), implies that

$$\chi = e_b^2 - 2\left(1 - e_b^2\right) j(2j + \cos i) > 0. \tag{31}$$

But χ is a constant of motion and so this equation also holds at any point on the critical orbit. For negative values of χ, the stationary point in the $\ell_x = 0$ plane does not exist. The condition $\chi > 0$ is satisfied for sufficiently small values of j or high values of $e_{\rm b}$ close to unity.

When $\chi > 0$ we have that the $\mathrm{d}\boldsymbol{\ell}/\mathrm{d}\tau = 0$ on the $\ell_x = 0$ plane. This means that the orbit has a cusp for $\phi = 0^\circ$ and 180°. For $\chi < 0$, there is still a cusp on the critical librating orbit. However, the cusp does not occur on the $\ell_x = 0$ plane. Fig. 12 plots the orbits of two cases with different values of χ. Both plots are for a system with $e_{\rm b0} = 0.5$. The upper plot has $j_0 = 0.1$, while the lower plot has $j_0 = 0.3$. The middle panel of Fig. 13 shows the critical angles for these cases.

The upper plot of Fig. 12 that has $\chi > 0$ has cusp points at $\phi = 0^\circ$ and 180° as expected. The critical librating orbit then covers a large 180° range of ϕ. The lower plot with $\chi < 0$ has cusp points (denoted as points $B_\pm$) that cover a much smaller range in ϕ.

Libration requires that $H < H_{\rm cr}$. We then obtain the condition

$$\Lambda_1 = -\left(1-e_{\rm b}^2\right)(2j+\cos i)^2 + 5e_{\rm b}^2 \sin^2 i \sin^2\phi > 0, \tag{32}$$

where we use $\ell_x = \sin\phi \sin i$ and $\ell_z = \cos i$ in evaluating H. For a massless ring we have that $j = 0$ and we recover equation 51 of Zanazzi & Lai (2018).

The minimum possible tilt for libration occurs where $\phi = 90^\circ$. To find the minimum possible tilt i for libration to occur given values of $e_{\rm b0}$ and j_0, we use equation (32) with $\phi = 90^\circ$ and $\Lambda_1 = 0$ to obtain

$$\cos i_{\rm min} = \frac{\sqrt{5} e_{\rm b0} \sqrt{4e_{\rm b0}^2 - 4j_0^2\left(1-e_{\rm b0}^2\right) + 1} - 2j_0\left(1-e_{\rm b0}^2\right)}{1+4e_{\rm b0}^2}. \tag{33}$$

For small j_0, the above equation can be expanded as a series to linear order in j_0 to give

$$\sin i_{\rm min} \simeq \sqrt{\frac{1-e_{\rm b0}^2}{1+4e_{\rm b0}^2}}\left(1 + \frac{2\sqrt{5} e_{\rm b0}\, j_0}{\sqrt{1+4e_{\rm b0}^2}}\right). \tag{34}$$

For a massless ring we have that $j_0 = 0$ and $e_{\rm b} = e_{\rm b0}$ (constant binary eccentricity), and we recover the minimum tilt angle given in equation 2 of Doolin & Blundell (2011). The term proportional to j_0 shows that the minimum angle for libration increases with ring angular momentum for small j_0.

For high binary eccentricity, $e_{\rm b0}$ close to unity, we have to lowest order in $1 - e_{\rm b0}$ that

$$\sin i_{\rm min} \simeq \sqrt{\frac{2}{5}}(1+2j_0)\sqrt{1-e_{\rm b0}}. \tag{35}$$

For large j_0 in this equation, libration can occur over a wide range of tilt angles provided that $e_{\rm b0} \gtrsim 1 - 5/(8j_0^2)$.

3.3.2 *Higher* j*/lower* ef$_b$ *branch*

The results in Section 3.3.1 are based on a critical librating orbit that passes through a stationary point (where $\mathrm{d}\boldsymbol{\ell}/\mathrm{d}\tau = 0$) that has the property that $\ell_x = 0$. These results apply for $\chi \geq 0$ in equation (31), which is based on the requirement that the binary eccentricity be a real quantity in equation (26). For larger j or lower $e_{\rm b}$ values, where $\chi < 0$, there does not exist a stationary point with $\ell_x = 0$. Instead, as we show below, the critical librating orbit for such larger j_0 cases involves a stationary point with the property that $e_{\rm bs} = 0$. The properties of this stationary point are also discussed in section A2 of Farago & Laskar (2010).

From equation (24) with $e_{\rm bs} = 0$, we have that

$$\ell_{zs} = \frac{\gamma^2 - \gamma_{\rm r}^2 - 1}{2\gamma_{\rm r}}. \tag{36}$$

Using equation (28) for the Hamiltonian, we have that its value at this stationary point for the critical librating orbit is then

$$H_{\rm cr} = \left(\frac{\gamma^2 - \gamma_{\rm r}^2 - 1}{2\gamma_{\rm r}}\right)^2. \tag{37}$$

We proceed as in Section 3.3.1 through the use of equations (11) and (24) in equation (37) and require that $H < H_{\rm cr}$ for a librating orbit to obtain the condition that

$$\Lambda_2 = e_{\rm b}^2 + 4j\left(1-e_{\rm b}^2\right)(-\cos i + j(-2+5\sin^2 i \sin^2\phi)) > 0, \tag{38}$$

which is valid for $\chi < 0$ in equation (31). The condition $\chi < 0$ is satisfied for sufficiently large values of j or small values of $e_{\rm b}$.

To find the minimum possible tilt i for libration to occur given values of $e_{\rm b0}$ and j_0, we use equation (38) with $\phi = 90^\circ$ and $\Lambda_2 = 0$ to obtain

$$\cos i_{\rm min} = \frac{\sqrt{\left(1-e_{\rm b0}^2\right)\left(1+4e_{\rm b0}^2+60\left(1-e_{\rm b0}^2\right)j_0^2\right)} - \left(1-e_{\rm b0}^2\right)}{10\left(1-e_{\rm b0}^2\right)j_0}. \tag{39}$$

In the limit of large j_0, we have to first order

$$\cos i_{\rm min} \simeq \sqrt{\frac{3}{5}} - \frac{1}{10 j_0}, \tag{40}$$

which approaches the critical angle for Kozai–Lidov oscillations as j_0 goes to infinity.

3.3.3 *Summary of analytical conditions for polar alignment*

Suppose we have a system with the following parameters at some instant in time: ring-to-binary angular momentum ratio $j = J_{\rm r}/J_{\rm b}$, mutual binary-ring inclination i, and longitude of ascending node for the ring ϕ. If $\chi > 0$ in equation (31), then equation (32) determines whether the system undergoes libration. If $\chi < 0$, then equation (38) determines whether the system undergoes libration. Libration in turn can lead to alignment to a stationary (polar) configuration.

The dotted lines in Fig. 13 are the minimum tilt angles for libration $i_{\rm min}$ obtained by numerically integrating the tilt evolution equations (7)–(10). (The minimum possible tilt for libration occurs where angle $\phi = 90^\circ$.) The values of $i_{\rm min}$ given analytically by equation (33) are plotted with solid red lines in Fig. 13 over the range of j_0 values where $\chi > 0$ in equation (31). The values of $i_{\rm min}$ given analytically by equation (39) are plotted with solid green lines in Fig. 13 over the range of j_0 values where $\chi < 0$. Notice that the red and green lines pass through the dotted lines, indicating excellent numerical agreement between the two independent methods (numerical and analytical) for determining minimum angles for both branches. Notice also that there is a change in behaviour of the minimum tilt angle near the largest value of j_0 plotted in red that occurs where $\chi = 0$. Fig. 12 shows a major change in orbital behaviour for the librating orbits with a change in sign of χ. Fig. 13 shows that for $\chi < 0$ (beyond the red lines), the minimum tilt does not increase as rapidly with j_0 and decreases for sufficient large j_0, as is also indicated by equation (40).

3.4 Comparison of the analytical criteria to the hydrodynamical simulations

3.4.1 Stationary inclination

Fig. 4 shows the ratio of the disc angular momentum to the binary angular momentum for some of the hydrodynamical simulations. The high-mass disc simulations ($M_d = 0.05\,M$) with binary eccentricity $e_b = 0.5$ have initially $J_d/J_b = 0.42$. In the analytical model in Fig. 11, this corresponds to a stationary inclination of $i_s = 69.7°$. This is close to the inclination that the hydrodynamic discs oscillate about (as shown the bottom right panel of Fig. 2 for initial inclination 60° and the bottom right panel of Fig. 7 for initial inclination of 80°).

For the larger eccentricity binary, $e_b = 0.8$, with the same disc parameters (Fig. 8), the system has angular momentum ratio initially $J_d/J_b = 0.61$ and in the analytical model in Fig. 11, this corresponds to a stationary inclination of $i_s = 80.6°$. This is in good agreement with the simulations shown in the top right and bottom left and right-hand panels of Fig. 8 that are librating.

The simulation with the larger disc size (outer radius $10\,a$) in the bottom right panel of Fig. 9 (run20), has initially $J_d/J_b = 0.52$. In the analytical model this corresponds to a stationary inclination of $i_s = 67.1°$. The largest disc size we considered (outer radius $20\,a$) in Fig. 10 (run21), has initially $J_d/J_b = 0.68$ and this corresponds to $i_s = 64.0°$.

The stationary inclination for the disc is consistently slightly less than the value predicted for the ring in Fig. 11. However, the angular momentum of the disc and the binary evolve in the disc simulations. While the ratio oscillates because the angular momentum of the binary oscillates, the angular momentum of the disc generally decreases in time. Furthermore, as described in the Introduction, the dynamics of a ring are somewhat different from that of an extended disc.

3.4.2 Condition for polar evolution

For the simulations described in Section 2.4.1 for binary eccentricity $e_b = 0.5$ and a high-mass disc $M_d = 0.05\,M$, the transition from librating to circulating solutions is in the range 50−60°. This system has angular momentum ratio $J_d/J_b = 0.42$. The critical inclination between librating and circulating solutions for this high disc angular momentum in the analytical model is 51° using equation (39). For the same disc parameters except disc mass $0.001\,M$, we previously found that the critical angle was in the range 40−50° (Martin & Lubow 2018). This system has angular momentum ratio $J_d/J_b = 0.0084$. In the analytical model for low angular momentum ratio, the critical angle for this angular momentum ratio is 38.4° (equation 39). The analytical model slightly underestimates the critical angle.

4 DISCUSSION

The polar aligned disc observed in HD 98800 by Kennedy et al. (2019) is within 4° of being perpendicular to the binary orbital plane. The binary has a semimajor axis of $a_b = 1$ au, eccentricity $e_b \simeq 0.785$, and the circumbinary gas disc in carbon monoxide extends from about 1.6 au out to about 6.4 au. Note that polar aligned discs have a smaller inner truncation radius than a disc aligned to the binary orbital plane (Franchini, Lubow & Martin 2019b). The binary component masses are 0.699 and 0.582 $M_\odot$ (Boden et al. 2005). We assume that the disc has evolved to a stationary configuration with tilt i_s given by equation (17). In making this assumption, we are assuming that this equation holds for a radially wide disc with viscosity.

Using the equation (17), we obtain an analytical expression for the ring (or disc) to binary angular momentum ratio $j = J_r/J_b$,

$$j = \frac{\left(1 + 4e_b^2\right)\cos i_s}{3\left(1 - e_b^2\right) - 5\cos^2 i_s}. \tag{41}$$

We apply the lower limit to the tilt $i_s = 86°$ and $e_b = 0.785$ to the above and obtain

$$J_r \simeq 0.21\,J_b. \tag{42}$$

Assuming the disc density falls off inversely with radius as R^{-q} and using the disc inner and outer radii values, we have that

$$J_r = k M_r\, a_b^2 \Omega_b, \tag{43}$$

where Ω_b is the binary orbital frequency, and M_r is the mass of the ring. Quantity k varies from 2.1 to 1.9 as q varies from 0 to 1.5. Using the properties of the binary cited above, we have that

$$J_b = 0.15 M a_b^2 \Omega_b. \tag{44}$$

Combining equations (42), (43), and (44), we have that $M_r \simeq 0.016M$. The disc (or ring) mass could be smaller if the tilt is less than 4° from perpendicular. Therefore, the disc mass must be $\lesssim 0.016M \approx 0.021\,M_\odot$, since the mass of the binary is $1.28\,M_\odot$. This mass range is quite plausible for protostellar discs.

Solid bodies may form within a gaseous disc that reaches its stationary inclination $i_s < 90°$. Such bodies will likely remain within the gaseous disc due to gravitational coupling, unless they are massive enough to open gaps. As the gas disc dissipates, its tilt angle can increase until it reaches the polar state at 90° misalignment with respect to the binary. The orbits of the solid bodies will likely remain coplanar with the disc again due to gravitational coupling, however, once the gaseous disc mass becomes sufficiently small this coupling will break down and the solid bodies may decouple from the gas disc before it reaches its final value of 90° inclination. Once the solid bodies break free of the gas disc their libration speeds will no longer be coordinated and they will randomize relative to each other. The random velocities could affect the planet formation process. Just how this operates is beyond the scope of this paper.

5 CONCLUSIONS

In this work, we have investigated the conditions under which the nodal libration mechanism can operate in a protostellar disc around an eccentric binary as first described by Martin & Lubow (2017). We apply both SPH simulations and analytical methods. Such discs undergo oscillations of the tilt and longitude of ascending node, similar to test particle orbits. However, for the case of a disc, dissipation leads to polar alignment of the disc. We have investigated the effect of a non-zero mass disc on the system evolution. The mass of the disc affects the outcome of the process because the binary evolution is affected. The disc affects the binary orbit gravitationally and through advection of mass and angular momentum. The binary eccentricity and tilt oscillate. The eventual alignment of disc with non-zero mass is at an angle less than 90°. This has significant implications for planet formation around eccentric binaries and for the detection properties of such discs.

We applied the secular evolution equations of Farago & Laskar (2010) to determine conditions related to the polar alignment of an arbitrary mass ring that orbits around an eccentric orbit binary. We determined the stationary misalignment angle, the generalized

polar angle, between the ring and binary as a function of system parameters. In the presence of dissipation, the ring tilt could evolve to this angle. This angle, given analytically by equations (17) and (18), decreases monotonically with increasing ratio of ring-to-binary angular momentum and decreasing binary eccentricity (see Fig. 11). A very small mass ring lies perpendicular to the binary orbit plane in the stationary configuration.

We applied the stationary tilt angle equation (17) to constrain the mass of the circumbinary disc in HD 98800 (see Section 4). We note that this condition is based on gravitational torques only and ignores the accretional torque on to the binary. Furthermore, it models the disc as a narrow ring. We did find however that SPH simulations appear to be in good agreement with the predictions of equation (17) (Section 3.4.1). In any case, we found this equation implies that the disc mass is less than about $0.02\,M_\odot$, in the range of typical protostellar disc masses. More accurate observational determinations of the tilt angle would be of benefit.

We determined analytical criteria required for a ring with mass to evolve to a generalized polar configuration (see Section 3.3.3) and determined the minimum misalignment inclination angles (see Fig. 13). For small values of the disc-to-binary angular momentum ratio j_0, the minimum tilt angle increases with j_0. But for larger j_0, this angle decreases. The change in behaviour is understood in terms of a transition between different types of stationary points for marginally librating orbits. As discussed in Section 3.4, we found approximate agreement between the results of the SPH simulations and the analytical model.

ACKNOWLEDGEMENTS

We thank Daniel Price for providing the PHANTOM code for SPH simulations and acknowledge the use of SPLASH (Price 2007) for the rendering of the figures. SHL acknowledges useful discussions with Gordon Ogilvie. We acknowledge support from NASA through grants NNX17AB96G and 80NSSC19K0443. Computer support was provided by UNLV's National Supercomputing Center.

REFERENCES

Aly H., Dehnen W., Nixon C., King A., 2015, MNRAS, 449, 65
Aly H., Lodato G., Cazzoletti P., 2018, MNRAS, 480, 4738
Armitage P. J., Livio M., 1996, ApJ, 470, 1024
Armitage P. J., Natarajan P., 2005, ApJ, 634, 921
Aronow R. A. et al., 2018, AJ, 155, 47
Artymowicz P., Clarke C. J., Lubow S. H., Pringle J. E., 1991, ApJ, 370, L35
Artymowicz P., Lubow S. H., 1994, ApJ, 421, 651
Artymowicz P., Lubow S. H., 1996, ApJ, 467, L77
Bate M. R., 2018, MNRAS, 475, 5618
Bate M. R., Bonnell I. A., Bromm V., 2003, MNRAS, 339, 577
Bate M. R., Lodato G., Pringle J. E., 2010, MNRAS, 401, 1505
Batygin K., Morbidelli A., Tsiganis K., 2011, A&A, 533, A7
Boden A. F. et al., 2005, ApJ, 635, 442
Boss A. P., 2006, ApJ, 641, 1148
Brinch C., Jørgensen J. K., Hogerheijde M. R., Nelson R. P., Gressel O., 2016, ApJ, 830, L16
Capelo H. L., Herbst W., Leggett S. K., Hamilton C. M., Johnson J. A., 2012, ApJ, 757, L18
Chiang E. I., Murray-Clay R. A., 2004, ApJ, 607, 913
Clarke C. J., Pringle J. E., 1993, MNRAS, 261, 190
Cuello N. et al., 2019, MNRAS, 483, 4114
Czekala I., Chiang E., Andrews S. M., Jensen E. L. N., Torres G., Wilner D. J., Stassun K. G., Macintosh B., 2019, ApJ, 883, 22
Doolin S., Blundell K. M., 2011, MNRAS, 418, 2656
Facchini S., Lodato G., Price D. J., 2013, MNRAS, 433, 2142
Farago F., Laskar J., 2010, MNRAS, 401, 1189
Ferrer S., Osacar C., 1994, Celest. Mech. Dyn. Astron., 58, 245
Foucart F., Lai D., 2013, ApJ, 764, 106
Foucart F., Lai D., 2014, MNRAS, 445, 1731
Franchini A., Lubow S. H., Martin R. G., 2019b, ApJ, 880, L18
Franchini A., Martin R. G., Lubow S. H., 2019a, MNRAS, 485, 315
Fu W., Lubow S. H., Martin R. G., 2015a, ApJ, 807, 75
Fu W., Lubow S. H., Martin R. G., 2015b, ApJ, 813, 105
Fu W., Lubow S. H., Martin R. G., 2017, ApJ, 835, L29
Kennedy G. M. et al., 2012, MNRAS, 421, 2264
Kennedy G. M. et al., 2019, Nat. Astron., 3, 230
Kozai Y., 1962, AJ, 67, 591
Larwood J. D., Papaloizou J. C. B., 1997, MNRAS, 285, 288
Lidov M. L., 1962, Planet. Space Sci., 9, 719
Lidov M. L., Ziglin S. L., 1976, Celest. Mech., 13, 471
Lodato G., Facchini S., 2013, MNRAS, 433, 2157
Lodato G., Price D. J., 2010, MNRAS, 405, 1212
Lodato G., Pringle J. E., 2007, MNRAS, 381, 1287
Lubow S. H., Artymowicz P., 1992, in Duquennoy A., Mayor M., eds, Binaries as Tracers of Star Formation. p. 145
Lubow S. H., Martin R. G., 2016, ApJ, 817, 30
Lubow S. H., Martin R. G., 2018, MNRAS, 473, 3733
Lubow S. H., Martin R. G., Nixon C., 2015, ApJ, 800, 96
Lubow S. H., Ogilvie G. I., 2000, ApJ, 538, 326
Martin R. G., Lubow S. H., 2017, ApJ, 835, L28
Martin R. G., Lubow S. H., 2018, MNRAS, 479, 1297
Martin R. G., Lubow S. H., Nixon C., Armitage P. J., 2016, MNRAS, 458, 4345
Martin R. G., Nixon C., Lubow S. H., Armitage P. J., Price D. J., Doğan S., King A., 2014, ApJ, 792, L33
Mayer L., Wadsley J., Quinn T., Stadel J., 2005, MNRAS, 363, 641
McKee C. F., Ostriker E. C., 2007, ARA&A, 45, 565
Miranda R., Lai D., 2015, MNRAS, 452, 2396
Miranda R., Muñoz D. J., Lai D., 2017, MNRAS, 466, 1170
Monin J.-L., Clarke C. J., Prato L., McCabe C., 2007, Protostars and Planets V. Univ. Arizona Press, Tucson, AZ, p. 395
Muñoz D. J., Miranda R., Lai D., 2019, ApJ, 871, 84
Mösta P., Taam R. E., Duffell P. C., 2019, ApJ, 875, L21
Nealon R., Price D. J., Nixon C. J., 2015, MNRAS, 448, 1526
Nelson A. F., 2000, ApJ, 537, L65
Nixon C., King A., Price D., 2013, MNRAS, 434, 1946
Nixon C., King A., Price D., Frank J., 2012, ApJ, 757, L24
Nixon C., Lubow S. H., 2015, MNRAS, 448, 3472
Nixon C. J., 2012, MNRAS, 423, 2597
Nixon C. J., King A. R., 2012, MNRAS, 421, 1201
Nixon C. J., King A. R., Pringle J. E., 2011, MNRAS, 417, L66
Papaloizou J. C. B., Terquem C., 1995, MNRAS, 274, 987
Picogna G., Marzari F., 2015, A&A, 583, A133
Price D. J., 2007, Publ. Astron. Soc. Aust., 24, 159
Price D. J., 2012, J. Comput. Phys., 231, 759
Price D. J., Federrath C., 2010, MNRAS, 406, 1659
Price D. J. et al., 2018, Publ. Astron. Soc. Aust., 35, e031
Shakura N. I., Sunyaev R. A., 1973, A&A, 24, 337
Shi J.-M., Krolik J. H., Lubow S. H., Hawley J. F., 2012, ApJ, 749, 118
Smallwood J. L., Lubow S. H., Franchini A., Martin R. G., 2019, MNRAS, 486, 2919
Verrier P. E., Evans N. W., 2009, MNRAS, 394, 1721
Williams J. P., Cieza L. A., 2011, ARA&A, 49, 67
Winn J. N., Holman M. J., Johnson J. A., Stanek K. Z., Garnavich P. M., 2004, ApJ, 603, L45
Xiang-Gruess M., 2016, MNRAS, 455, 3086
Zanazzi J. J., Lai D., 2018, MNRAS, 473, 603

APPENDIX A: STATIONARY TILT

We derive the conditions for the stationary tilt of the ring relative to the binary given in equations (15)–(17) of Section 3.2. We apply the stationary (fixed point) conditions of zero time derivatives (equations 13 and 14) to the tilt and binary eccentricity evolution equations (7)–(10). In addition, we apply the condition that $\ell_y = 0$, since we are interested in tilts in the x–z plane. Equations (7), (9), and (10) are trivially satisfied for zero time derivatives. Only equation (8) for $\mathrm{d}\ell_y/\mathrm{d}\tau$ needs to be considered. This equation implies

$$\ell_x \left[\left(1 + 4e_\mathrm{b}^2\right) \ell_z + \frac{\gamma_\mathrm{r}}{\sqrt{1 - e_\mathrm{b}^2}} \left(\left(1 - e_\mathrm{b}^2\right) \left(2 - 5\ell_x^2\right) + 5e_\mathrm{b}^2 \ell_z^2 \right) \right] = 0. \tag{A1}$$

The solution with $\ell_x = 0$ corresponds to a coplanar system with the ring rotating either prograde ($\ell_z = 1$) or retrograde ($\ell_z = -1$) relative to the binary.

For ℓ_x non-zero, the bracketed term in equation (A1) is zero, resulting in the same equation as equation A16 of appendix A4 in Farago & Laskar (2010) with some obvious changes in variable names. We use the fact that $|\boldsymbol{\ell}| = \ell = 1$ to eliminate ℓ_x using $\ell_x^2 = 1 - \ell_z^2$. Equation (A1) can then be solved analytically as a quadratic equation in ℓ_z to obtain two roots

$$\ell_z = \frac{-(1 + 4e_\mathrm{b}^2) \pm \sqrt{\left(1 + 4e_\mathrm{b}^2\right)^2 + 60 \left(1 - e_\mathrm{b}^2\right) j^2}}{10 j}. \tag{A2}$$

The solution with the positive sign for the square root has the property that ℓ_z goes to zero as j goes to zero. That is, a low-mass ring is nearly perpendicular to the binary orbital plane. This solution is of interest for the purposes of this paper and is used in the text as equation (17).

The solution with the minus sign for the square root applies to retrograde rings, since $\ell_z < 0$. The requirement that $\ell_z > -1$ implies that

$$j > \frac{1 + 4e_\mathrm{b}^2}{2 + 3e_\mathrm{b}^2}. \tag{A3}$$

In the limit of large j, we have that

$$\ell_z = -\sqrt{\frac{3\left(1 - e_\mathrm{b}^2\right)}{5}}. \tag{A4}$$

With increasing j, tilt component ℓ_z increases monotonically from -1 to the value given by equation (A4). We do not consider the applications of this stationary solution in this paper.

This paper has been typeset from a TEX/LATEX file prepared by the author.